Texturing in the Earth's inner core due to preferential growth in its equatorial belt

Renaud Deguen, Philippe Cardin, Sebastien Merkel, R.A. Lebensohn

Texturing in the Earth's inner core due to preferential growth in its equatorial belt

Renaud Deguen[a,b], Philippe Cardin[a,*], Sébastien Merkel[c], Ricardo A. Lebensohn[d]

[a] *Institut des Sciences de la Terre (ISTerre), CNRS, Université Joseph-Fourier Grenoble 1, Grenoble, France.*
[b] *Earth and Planetary Sciences, Johns Hopkins University, Baltimore, Maryland, USA.*
[c] *Unité Matériaux et Transformations (UMET), CNRS, Université Lille 1, Villeneuve d'Ascq, France.*
[d] *Materials Science and Technology Division, Los Alamos National Laboratory, Los Alamos, New Mexico, USA.*

Abstract

We propose an extension of the model by Yoshida et al. (1996), where deformation in the inner core is forced by preferential growth in the equatorial belt, by taking into account the presence of a stable compositional stratification. Stratification inhibits vertical motion, imposes a flow parallel to isodensity surfaces, and concentrates most deformation in a shallow shear layer of thickness $\sim B^{-1/5}$, where B is the dimensionless buoyancy number. The localization of the flow results in large strain rates and enable the development of a strong texture of iron crystals in the upper inner core. We couple our dynamical model with a numerical model of texture development and compute the time evolution of the lattice preferred orientation of different samples in the inner core. With sufficient stratification, texturing is significant in the uppermost inner core. In contrast, the deeper inner core is

*Corresponding author
Email address: philippe.cardin@ujf-grenoble.fr (Philippe Cardin)

unaffected by any flow and may preserve a fossil texture. We then investigate the effect of an initial texture resulting from solidification texturing at the ICB. In the present inner core, the deformation rate in the shallow shear layer is large and can significantly alter the solidification texturing, but the solidification texture acquired early in the inner core history can be preserved in the deeper part. Using elastic constants from *ab initio* calculations, we predict different maps of anisotropy in the modern inner core. A model with both solidification texturing and subsequent deformation in a stratified inner core produce a global anisotropy in agreement with seismological observations, both in magnitude and geographical distribution, with a weak anisotropy in the uppermost layer and stronger anisotropy in the deeper parts.
Keywords: inner core, anisotropy, HCP iron, texturation, crystallization

1. Introduction

The inner core of the Earth exhibits a noticeable anisotropy in P-wave velocity and attenuation (Poupinet et al., 1983; Morelli et al., 1986; Woodhouse et al., 1986; Souriau, 2007), which may reflect structural and/or dynamical complexity. The main observation is a $\sim$ 3% anisotropy with cylindrical symmetry, with the fast axis aligned with the axis of rotation of the Earth or possibly sligthly tilted (Su et al., 1996). The degree of inner core anisotropy is increasing with depth (Souriau, 2003), with no strong anistropy in the upper 150-200 km (Song and Helmberger, 1995), and perhaps still different [but poorly constrained (Calvet et al., 2006)] seismic properties in an innermost inner core (Ishii and Dziewoński, 2002; Niu and Chen, 2008). There is also a growing consensus on the presence of an hemispherical asymmetry in the seis-

mic properties of the upper part of the inner core (Tanaka and Hamaguchi, 1997): the Western hemisphere (west of the Greenwich meridian) appears more anisotropic than the Eastern hemisphere. This observation can be due to lateral variations of the local seismic properties (Niu and Wen, 2001), because of a different degree of crystal alignment, for instance, or as originating from a longitudinal variation of the thickness of the quasi-isotropic upper layer, which would have to vary from $\sim$ 100 km in the western hemisphere to $\sim$ 400 km in the eastern hemisphere (Garcia and Souriau, 2000). An anisotropy in inner core seismic attenuation is also observed (Souriau and Romanowicz, 1996, 1997; Yu and Wen, 2006a) and shows hemispherical variations (Garcia, 2002; Yu and Wen, 2006b) in reminiscence with the pattern of the anisotropy.

The seismic anisotropy of the inner core is most often interpreted as resulting from the lattice preferred orientation (LPO) of elastically anisotropic iron crystals. Processes for creating iron LPO in the inner core include solidification at the inner core boundary (ICB) (Karato, 1993; Bergman, 1997; Brito et al., 2002), plastic deformation (Jeanloz and Wenk, 1988; Karato, 1999; Wenk et al., 2000; Buffett and Wenk, 2001), or stress-induced recrystallization (Yoshida et al., 1996). It is not, however, unlikely that a combination of several mechanisms are - or have been - active. To what extent solidification texturing can be reworked by subsequent deformation might well be a critical point to understand the observed radial variations in anisotropy and attenuation.

A number of deformation models have been proposed, including thermal convection (Jeanloz and Wenk, 1988; Wenk et al., 1988, 2000; Weber and

Machetel, 1992; Buffett, 2009), continuous deformation forced by aspherical growth (Yoshida et al., 1996), and flow induced by the outer core magnetic field (Karato, 1999; Buffett and Wenk, 2001). Most of these mechanisms have significant drawbacks. In particular, their viability depends on the thermal and chemical state of the inner core. Apart from the mechanism of Buffett and Wenk (2001), all involve a large radial flow (Jeanloz and Wenk, 1988; Yoshida et al., 1996; Karato, 1999; Wenk et al., 2000) and will be inhibited by a stable stratification in the inner core (Buffett and Bloxham, 2000; Deguen and Cardin, 2009).

In this study, we concentrate our efforts on connecting geodynamics and simulations of LPO development in mineral aggregates using the viscoplastic self-consistent (VPSC) method of Lebensohn and Tome (1993). We will restrict ourself to a single phase of iron, hexagonal-closed-packed (*hcp*-Fe), using a single set of plastic deformation mechanisms, described therein, and a single set of elastic moduli (Vočadlo et al., 2009). We extend the dynamical model proposed by Yoshida et al. (1996) to include stable density stratification in the inner core (Deguen and Cardin, 2009), and simulate the development of LPO associated with the deformation.

In part 2, we briefly discuss the thermal and chemical states of the inner core, and introduce our dynamical model. This inner core model couples preferential crystallization in the equatorial region (Yoshida et al., 1996) and density stratification. The density stratification arises from inner core growth and evolution of the concentration of light elements in the fluid outer core over time (Deguen and Cardin, 2009). In part 3, from our numerical models of core formation, we track the deformation history of markers inside the

inner core and calculate the evolution of LPO in Fe using the VPSC method. In part 5, using published value of elastic moduli of *hcp*-Fe, we produce maps of P wave velocity anisotropy in the modern inner core.

2. Dynamical model

In this study, we focus on the effect of thermal or chemical stratification on the dynamics of the inner core. The thermal state of the inner core is discussed in section 2.1, the chemical stratification is derived in 2.2, the dynamic equations are presented in 2.3, and the resulting computations are discussed in 2.4.

2.1. Thermal state of the inner core

The thermal state of the inner core results from a competition between cooling at the ICB and extraction of the inner core internal heat. The inner core would be stably stratified (subadiabatic) if its growth is slow enough to allow thermal conduction to evacuate most of the internal heat. Deguen and Cardin (2009) introduced a simplified criterion for thermal stability in the inner core, which is based on the assumption that the cooling rate of the core is constant (A similar approach has been given by Buffett (2009)). In this model, the geotherm in the inner core is subadiabatic (stably stratified) if

$$\tau_{\rm ic} > \tau_\kappa \left(\frac{dT_s}{dT_{\rm ad}} - 1 \right), \tag{1}$$

where $\tau_{\rm ic}$ is the age of the inner core, $\tau_\kappa = r_{\rm icb}^2(\tau_{\rm ic})/(6\kappa)$ is the present thermal diffusion time, r_{icb} is the radius of the inner core, κ the thermal diffusivity, and $dT_s/dT_{\rm ad}$ the ratio of the Clapeyron slope to the adiabat. This criterion

provides a first-order estimate of the age of the inner core required for thermal stratification and explicitly describes the sensitivity of the thermal stratification limit to the relevant parameters. Moreover, it is shown in Deguen and Cardin (2011) that this criterion remains valid when a more realistic model of core thermal history is used (Labrosse et al., 2001).

Uncertainties on τ_κ are mainly due to uncertainties on the thermal conductivity of iron at inner core conditions. The relatively large value ($k = 63$ W.m^{-1}.K^{-1} in the outer core at the ICB, $k = 79$ W.m^{-1}.K^{-1} in the inner core) favored by Stacey and Anderson (2001) has been recently revised downward by Stacey and Loper (2007). Stacey and Davis (2008) give $k = 36$ W.m^{-1}.K^{-1} for the inner core.

The ratio $dT_s/dT_{\rm ad}$ can be estimated by using Lindeman's law,

$$\frac{dT_s}{dP} = \frac{2(\gamma - 1/3)T}{K_T}, \tag{2}$$

and writing the adiabatic temperature gradient as

$$\frac{dT_{\rm ad}}{dP} = \frac{\gamma T}{K_S}, \tag{3}$$

where γ is the Gruneisen parameter, P the pressure, T the temperature, K_T and K_S the isothermal and adiabatic bulk modulus, respectively. Using the thermodynamic identity $K_S = K_T(1 + \gamma\alpha T)$, we find

$$\frac{dT_s}{dT_{\rm ad}} = \frac{2(\gamma - 1/3)(1 + \gamma\alpha T)}{\gamma}. \tag{4}$$

With the values and uncertainties of thermo-physical properties given in table 1, we find $\tau_\kappa = 1.4 \pm 0.7$ Gy, and $dT_s/dT_{\rm ad} = 1.65 \pm 0.11$. This gives a critical age for thermal stratification of 0.9 ± 0.6 Gy. The important point here is that the range of critical ages we obtain fully overlaps with what

models of core thermal evolution predict for the age of the inner core, e.g. 1 ± 0.5 Gy in Labrosse et al. (2001) and 1.15 ± 0.75 Gy in Nimmo (2007). This means that the uncertainties are such that whether the inner core is subadiabatic or superadiabatic is not known. In this paper, we assume that it is subadiabatic and that the inner core has a stable thermal stratification.

2.2. Chemical stratification in the inner core

The composition of the core remains uncertain. However, a comparison between outer core density (Dziewonski and Anderson, 1981) and that of liquid iron at core conditions (Laio et al., 2000) indicates that the outer core material is 6-10% lighter than pure iron. The presence of other elements is also inferred from seismological estimates of the density jump at the inner core boundary, $\Delta\rho_{icb} = 800 \pm 200$ kg m^{-3} (Masters and Gubbins, 2003; Souriau, 2007). The density jump due to solidification alone (≈ 200 kg m^{-3}, Laio et al. (2000)) is not sufficient to explain the observed value, implying that, as most alloys, the core mixture partitions upon freezing.

If the outer core is assumed to be well mixed, the evolution of the concentration of the light element $c^\ell(t)$ in the liquid outer core is given by the Rayleigh distillation law (*e.g.* Albarède, 1996),

$$c^\ell(t) = c_0^\ell \left[1 - \frac{M_{ic}(t)}{M_0}\right]^{D-1}, \tag{5}$$

where c_0^ℓ is the concentration in the core prior to inner core nucleation, M_{ic} the mass of the inner core, and M_0 the mass of the core. For simplicity, we approximate $M_{ic}(t)/M_0 \approx (r_{icb}(t)/r_c)^3$. The light element concentration in

Table 1: Parameters used in this study.

Parameter	Symbol	Value
Core radius [a]	r_{c}	3480 km
Inner core radius[a]	r_{icb}	1221 km
Solidification temperature [b]	T_{icb}	5600 ± 500 K
Gruneisen parameter [c]	γ	1.4 ± 0.1
Thermal expansivity [c]	α_T	$1.1 \pm 0.1 \times 10^{-5}$ K^{-1}
Heat capacity [d]	c_p	800 ± 80 J.kg^{-1}.K^{-1}
Density in the inner core [a]	ρ	13 000 kg.m^{-3}
Thermal conductivity [e]	k	$36 - 79$ W.m^{-1}.K^{-1}
Initial concentration [b]	c_0	5.6 wt%
Partition coefficient [b]	D	0.8
Chemical expansivity [f]	α_c	-1

[a] From PREM (Dziewonski and Anderson, 1981).

[b] From Alfè et al. (2002).

[c] From Vočadlo (2007).

[d] From Stacey and Davis (2008).

[e] From Stacey and Anderson (2001) and Stacey and Davis (2008).

[f] See text (section 2.2).

the inner core, $c(r)$ becomes

$$c(r) = Dc_0^\ell \left(1 - \left(\frac{r}{r_c}\right)^3\right)^{D-1}, \tag{6}$$

and the corresponding profile of differential compositional density is then

$$\Delta\rho_c = \alpha_c \rho [c(r) - c(0)], \tag{7}$$

$$= \alpha_c \rho D c_0^\ell \left[\left(1 - \left(\frac{r}{r_c}\right)^3\right)^{D-1} - 1\right], \tag{8}$$

$$\approx \alpha_c \rho D(1-D) c_0^\ell \left(\frac{r}{r_c}\right)^3, \tag{9}$$

where D is the partition coefficient (the ratio of the concentration in the solid to that in the liquid), ρ the mean density in the inner core, and $\alpha_c = (1/\rho)(\partial\rho/\partial c)$ is the compositional expansion coefficient. Equation (9) shows that the chemical stratification is approximately proportional to $D(1-D)$: stratification would be maximum if $D = 0.5$, and is small if the distribution coefficient is either small or close to one.

The stratification depends on the nature and abundance of the light elements present in the core. The composition of the core has been a long standing issue and is still controversial, but recent models favour O, Si and S as the most plausible alloying elements. *Ab initio* calculations of the partitioning behavior of O, Si and S by Alfè et al. (2002) suggest that Si and S both partition weakly (with similar partition coefficients, $D^{\mathrm{Si,S}} = 0.8$) while, in contrast, O partitions strongly, $D^{\mathrm{O}} = 0.02$ (values of D are converted from molar ratios to mass ratios). These values favor the presence of sulfur or silicium in the inner core. Alfè et al. (2002) estimate that the outer core contains 5.6 wt. % of Si and/or S and 2.5 wt. % of O, in good agreement

with the geochemical model of Allègre et al. (1995), and that the inner core contains 4.4 wt. % of Si/S and neglible amount of O. Badro et al. (2007) used additional constraints from experimentally measured compressional wave velocity of Fe-Si, Fe-S and Fe-O alloys. In their model, S is unlikely to be a major component of the inner core, the outer core contains 2.8 wt. % Si and 5.3 wt. % O, and the inner core is constituted of 2.3 wt. % Si and 0.1 wt. % O.

The chemical expansion coefficient can be estimated from the partial atomic volumes of Fe, Si, S and O calculated by Alfè et al. (2002). We find $\alpha_c^{\mathrm{Si}} = -0.91$, $\alpha_c^{\mathrm{S}} = -0.67$ and $\alpha_c^{\mathrm{O}} = -1.3$ in the limit $c \to 0$ (Deguen and Cardin, 2011).

With the distribution coefficients calculated by Alfè et al. (2002), the chemical models discussed above, and the estimates of α_c, we find that the density stratification associated with Si/S is much larger than that associated with O. Therefore, in our model, the inner core is considered as a Fe-(Si,S) binary mixture, with a distribution coefficient equal to 0.8. With the value listed in table 1, the different in density between the center of the Earth and in the ICB is $\Delta\rho_c \sim -5$ kg m^{-3}.

This model includes a number of approximations:

(i) The pressure and temperature dependence of the partition coefficient and the compositional expansion are neglected.

(ii) We also neglect possible variations of the effective partition coefficient resulting from changes in the efficiency of melt extraction by compaction (Sumita et al., 1996) and interdendritic convection (Loper, 1983; Worster, 1997) in a mushy layer at the ICB. As noted by Al-

boussière et al. (2010), this may significantly decrease the magnitude of the chemical stratification.

(iii) We suppose a perfect mixing in the outer core, thus ignoring the possible accumulation of a light element rich liquid below the CMB (Fearn and Loper, 1981) or the presence of a dense layer in the lowermost liquid outer core (Souriau and Poupinet, 1991; Alboussière et al., 2010).

(iv) Chemical interactions between melt in the outer core and silicate material at the CMB, which might buffer the composition of the outer core (Buffett et al., 2000), are assumed negligeable.

The compositional density variation of our model reflects a relative enrichment of light elements at the top of the inner core as it grows. It is the internal imprint of the enrichment of the outer core in those same light elements induced by the partitioning during the growth of the inner core. The variation of concentration of light element in the inner core generates an internal solute flux by diffusion. The solute diffusivity is not known but is unlikely to be much larger than the self-diffusion of iron, estimated below $10^{-12}\mathrm{m}^2.\mathrm{s}^{-1}$ in the inner core (Van Orman, 2004). Chemical diffusion is negligible as the diffusion time is larger than 10^6 Gyr for the inner core, and the compositional profile (9) is valid on the time scale of the inner core formation ($\approx$1 Gyr).

2.3. Dynamic equations for a stratified inner core

We build a model for a thermally and chemically stratified inner core according to the two previous subsections. In these conditions, the inner core stays at rest except if external forcings, such as pressure forcings (Yoshida

et al., 1996) or magnetic forcings (Karato, 1999; Buffett and Bloxham, 2000; Buffett and Wenk, 2001), are imposed. In this paper, we follow the ideas of Yoshida et al. (1996) and focus on how differential growth of the inner core generates motion in a stratified inner core. For simplicity, we consider only the chemical contribution to the density stratification.

2.3.1. Equatorial growth of the inner core

The growth of the inner core is primarily due to its cooling by action of convective motions in the liquid outer core, also responsible of the geodynamo generation. The predominance of the axial geomagnetic dipole throughout the Earth's history demonstrates the permanent key role of the Coriolis force in the fluid motion in the outer core. Thermal convection in the outer core is made of columnar vortices aligned with the axis of rotation. This quasi geostrophic flow, first predicted by Busse (1970) and later confirmed by numerical or experimental means (Zhang, 1992; Dormy et al., 2004; Cardin and Olson, 1994) has a strong influence on convective heat transfer (Aubert et al., 2008; Aurnou et al., 2008).

Accordingly, it is expected that more heat is extracted from the equatorial band than from the polar regions of the inner core by the geodynamo. Following Yoshida et al. (1996), we model this by introducing a spherical harmonic degree 2 dependence in the rate of crystallization of the inner core u,

$$u(\theta, t) = u_{icb}(t) \left(1 - S_2 \frac{3\cos^2\theta - 1}{2} \right), \tag{10}$$

where θ is the colatitude and S_2 is a dimensionless parameter that measures the differential growth. Calculations by Aubert et al. (2008) show a variation

of the ICB heat flux of +30% in the equatorial band and -30% in polar regions. In other words, the crystallization rate at the equator is approximately twice larger than that at the poles, which is equivalent to $S_2 = 2/5$.

Preferential growth of the inner core in the equatorial belt produces an out-of-equilibrium topography, which, if not sustained by heterogeneous solidification, would relax toward hydrostatic equilibrium. The problem is very similar to that of post-glacial rebound, and the timescale of viscous relaxation τ_η can be calculated by extending to spherical geometry the classical calculation of topography relaxation in a semi-infinite domain (*e.g.* Turcotte and Schubert, 2002). We find

$$\tau_\eta = \frac{19}{5}\frac{\eta}{\Delta\rho_{\rm icb} g r_{\rm icb}} \simeq \left(\frac{\eta}{10^{18}\ \text{Pa.s}}\right)\left(\frac{1221\ \text{km}}{r_{\rm icb}}\right)^2 \times 40\ \text{year}, \qquad (11)$$

where η is the dynamic viscosity of iron in the inner core, and g the acceleration of gravity. Since the relaxation timescale is very small in comparison to the timescale of boundary conditions evolution and inner core growth, the inner core topography must be in a quasi-steady state, with the growth rate anomaly balanced by the continuous relaxation of the ICB topography (Yoshida et al., 1996). The radial velocity at the ICB is therefore prescribed to be equal to the opposite of the anomalous solidification rate.

This gives boundary conditions for the radial velocity; boundary conditions for the horizontal velocity are given by the assumption that the ICB is a shear stress free boundary.

The newly crystallized material has a solute concentration $c(r_{icb}(t))$ given by (6).

2.3.2. Equations of motion in a growing inner core

We consider an incompressible fluid of constant viscosity η in a spherical domain ($r < r_{icb}$). The Boussinesq approximation is valid and the momentum equation is written as :

$$\mathbf{0} = -\boldsymbol{\nabla} p + \alpha_c \bar{\rho} c \mathbf{g} + \eta \boldsymbol{\nabla}^2 \mathbf{v}, \tag{12}$$

where p is the dynamic pressure, $\alpha_c c = (\rho - \bar{\rho})/\bar{\rho}$ is the density perturbation from the static density field. Inertial terms have been neglected as the Reynolds number of the flow is vanishingly small. Taking the curl of the Stokes equation (12) gives

$$\mathbf{0} = -\frac{\alpha_c \bar{\rho} g'}{\eta} \frac{\partial c}{\partial \theta} \mathbf{e}_\phi + \boldsymbol{\nabla}^2 \boldsymbol{\nabla} \times \mathbf{v}, \tag{13}$$

where g has been assumed to be linear in radius, and $g' = dg/dr$. Taking advantage of the incompressibility of the velocity field, we can introduce the poloidal (P) and the toroidal (T) scalars to describe the velocity field $\mathbf{v} = \boldsymbol{\nabla} \times (T\mathbf{r}) + \boldsymbol{\nabla} \times \boldsymbol{\nabla} \times (P\mathbf{r})$ which are projected onto the basis of the axisymmetric spherical harmonics $(P, T) = \sum (P_l(r), T_l(r)) Y_l^0(\theta)$. Taking $\mathbf{e_r} \cdot \boldsymbol{\nabla} \times (13)$ and $\mathbf{e_r} \cdot \boldsymbol{\nabla} \times \boldsymbol{\nabla} \times (13)$, we find

$$D_l^2 P_l = \frac{\alpha_c \bar{\rho} g' r}{\eta} c_l \quad \text{and} \quad D_l^2 T_l = 0, \tag{14}$$

where c_l is the degree l spherical harmonic component of the solute concentration field and D_l is the Laplacian operator defined by $\frac{\partial^2}{\partial r^2} + \frac{2}{r}\frac{\partial}{\partial r} - \frac{l(l+1)}{r^2}$.

At the ICB, we deduce from (14) and (10) that the toroidal flow is zero and that, consequently, the velocity field is fully described by its poloidal part. To write (14) in a dimensionless form, we scale the length by $r_{icb}(t)$, the velocity

by $u_{icb}(t)$ and the solute concentration by the difference of concentration $\Delta c(t) = c(r_{icb}) - c(0)$ between the concentration at the top of the growing inner core and the initial concentration at the center. The poloidal part of (14) becomes

$$D_l^2 \tilde{P}_l = B\tilde{c}_l, \tag{15}$$

where $\tilde{}$ stands for the dimensionless variables and B, the dimensionless buoyancy number, is defined as

$$B = \frac{\alpha_c \bar{\rho} g' \Delta c(t) r_{icb}^3(t)}{\eta u_{icb}(t)}. \tag{16}$$

B increases significantly during the growth of the inner core as a result of the combined effect of increasing stratification ($\Delta c \propto r_{icb}^3$ and $g \propto r_{icb}$), decreasing solidification rate, and increasing length scale r_{icb}, which makes the viscous transfert of momentum less efficient. If we assume that the inner core radius grows as the square root of time (simplified context of 2.1), B evolves as r_{icb}^7. Since α_c is negative, B is negative, which corresponds to a stratified stable system. The actual value of B in the inner core suffers from very large uncertainties on the solid-state viscosity of iron in those conditions (Yoshida et al., 1996; Buffett, 1997; Van Orman, 2004), with published estimates ranging from 10^{11} Pa.s to 10^{21} Pa.s. With $\Delta\rho_c = -5$ kg m^{-3} (see 2.2) and a typical $u_{icb} = 3 \times 10^{-11}$m.s^{-1} (1 mm/yr), the present value of B (noted $B^* = B(\tilde{t} = 1)$) would be

$$B^* = -10^6 \times \left(\frac{10^{18} \text{ Pa.s}}{\eta} \right). \tag{17}$$

We explore a large range of B value, going from $B = 0$ (no stratification, Yoshida et al. (1996)) to $B^* = -10^9$ (very stratified and moderately viscous inner core).

2.3.3. Light element transport equation

The solute transport equation is written as

$$\frac{\partial c}{\partial t} + \mathbf{v} \cdot \boldsymbol{\nabla} c = 0. \tag{18}$$

In order to simplify the numerical implementation, we solve the problem in a spherical domain with no moving boundary. This is done naturally with our choice of length scale which is the time dependent radius of the inner core $r_{icb}(t)$. The radial domain is defined by $\tilde{r} = r/r_{icb}(t) \in [0, 1]$ with a fixed boundary at $\tilde{r} = 1$. The time derivative in the new coordinates system $\tilde{\mathcal{R}}$ is written (Crank, 1984) as

$$\left.\frac{\partial}{\partial t}\right|_{\tilde{\mathcal{R}}} = \left.\frac{\partial}{\partial t}\right|_{\mathcal{R}} - \left.\frac{\partial \tilde{r}}{\partial t}\right|_{\mathcal{R}} \left.\frac{\partial}{\partial \tilde{r}}\right|_{t} = \left.\frac{\partial}{\partial t}\right|_{\mathcal{R}} + \tilde{r}\frac{u_{icb}}{r_{icb}} \left.\frac{\partial}{\partial \tilde{r}}\right|_{t}. \tag{19}$$

This allows the equation of solute transport to be written in the new referential as

$$\frac{\partial \tilde{c}}{\partial \tilde{t}} = \frac{u_{icb}\tau_{ic}}{r_{icb}} \left(\tilde{r}\, \tilde{\mathbf{e}}_{\mathbf{r}} - \tilde{\mathbf{v}}\right) \cdot \tilde{\boldsymbol{\nabla}} \tilde{c} - \frac{\dot{\Delta c}\, \tau_{ic}}{\Delta c} \tilde{c}, \tag{20}$$

where time has been scaled by the age of the inner core, τ_{ic}, and other variables as in section 2.3.2.

The first term in the RHS of equation (20) comes from the moving boundary transformation and corresponds to an apparent inward advection in the new referential. The last term in the RHS comes from the time dependence of the prescribed concentration scale $\Delta c(t)$ ($\dot{\Delta c}$ stands for the time derivative of Δc). If we assume that the inner core radius grows as the square root of time, and that the compositional evolution takes the simplified form (9), then $(u_{icb}\tau_{ic})/r_{icb} = 1/2$ and $(\dot{\Delta c}\, \tau_{ic})/\Delta c$ simplifies to $3/2$.

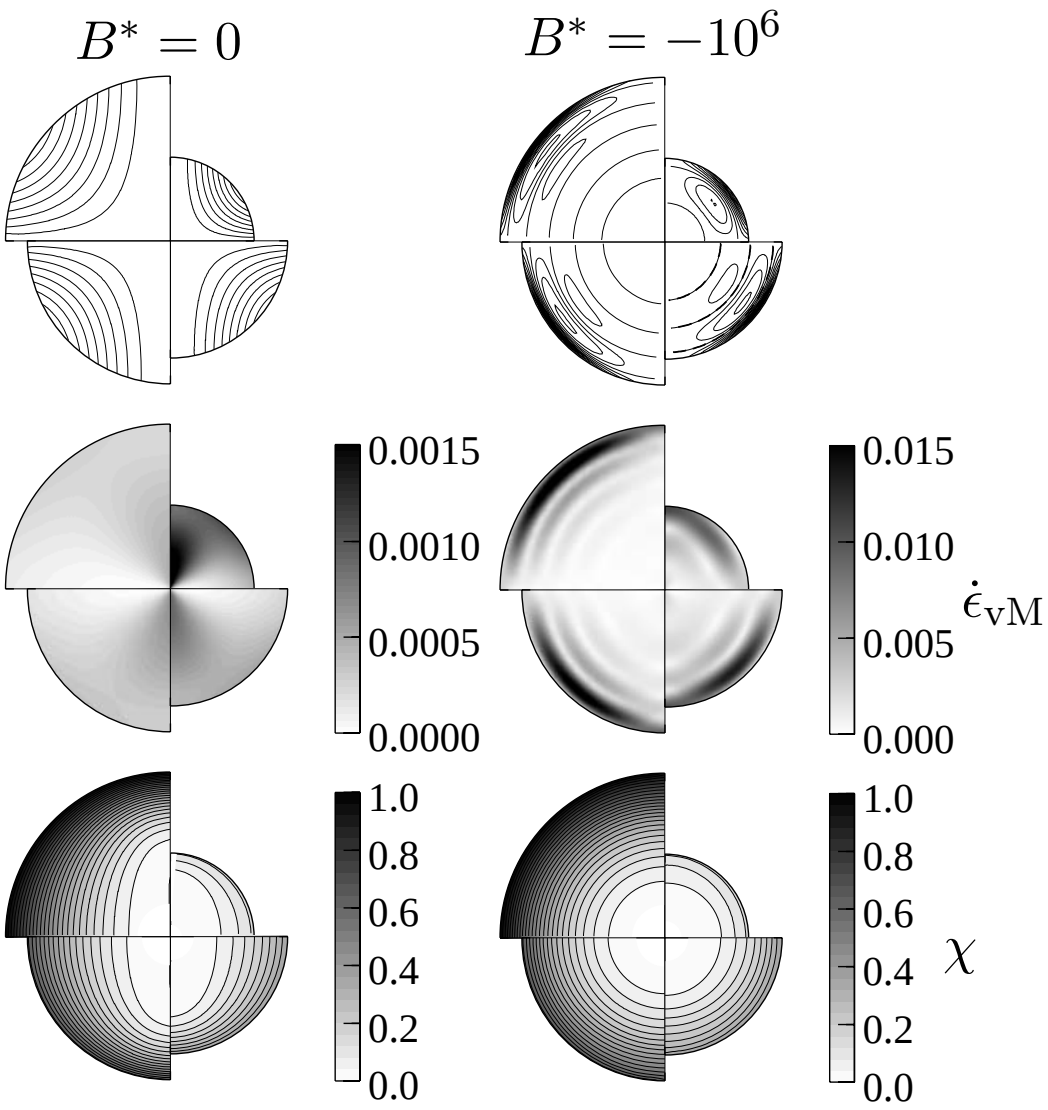

Figure 1: Time evolution of the flow induced by preferential growth of the inner core at the equator for two values of the dimensionless buoyancy number, $B^* = 0$ (no stratification) and $B^* = -10^6$ (stratified flow). All subfigures are divided into four quadrants, which correspond to non-dimensional times $\tilde{t} = 0.25$, 0.5, 0.75 and 1, starting clockwise from the upper right quadrant; the radius of each quadrant reflects the value of $r_{icb}(t)$. a, Contours of the stream function ψ. b, von Mises equivalent strain rate $\dot{\epsilon}_{\mathrm{vM}}$, in Myr^{-1}. c, Non-dimensional light-element concentration $\chi = c/\Delta c(\tilde{t} = 1)$. The computations were made with $S_2 = 2/5$, which corresponds to a solidification rate two times higher at the equator than at the poles.

2.3.4. Numerical implementation and simulations

We implement the two equations (15,20) into a meridional plane, with a spectral description for the horizontal dependence and a finite difference scheme for the radial description. The radial mesh can be contracted in the outermost part of the domain for large B. Boundary conditions at $\tilde{r} = 1$ are : $\forall l \neq 2, \tilde{P}_l = 0$, $\tilde{P}_2 = S_2$, and $\forall l$, $\frac{\partial^2 \tilde{P}_l}{\partial \tilde{r}^2} = [2 - l(l+1)]\tilde{P}_l$ (shear stress free condition), $\tilde{c_0} = 1$ and $\forall l \neq 0$, $\tilde{c}_l = 0$. The non linear term $\tilde{\mathbf{v}} \cdot \tilde{\boldsymbol{\nabla}} \tilde{c}$ is evaluated in the physical space at each timestep. A semi-implicit Crank-Nickolson scheme is implemented for the time evolution of the linear terms and an Adams-Bashforth procedure is used for the non-linear term. We typically use time steps of order 10^{-4}. This problem presents no major numerical difficulty.

We start the simulations with a small inner core ($\tilde{r} = 0.1$) and let evolve the system to the final time $\tilde{t} = 1$. We track some fluid particles to compute their trajectories and their stress tensor $\dot{\epsilon}$ by bilinear interpolation in the physical space. These quantities are saved and used as inputs for the mineralogical model.

To visualize the dynamic effect in the inner core, we plot the isocontours of the stream function ψ computed from the poloidal component of the axisymmetric velocity to exhibit the flow pattern, $\psi = r \sin\theta \frac{\partial P}{\partial \theta}$. The deformation is shown by the plot of the von Mises equivalent strain rate $\dot{\epsilon}_{\mathrm{vM}} = f(P)$ (a measure of the deviatoric strain rate (Tome et al., 1984; Wenk et al., 2000)). The normalised concentration of the solute $c/\Delta c(\tilde{t} = 1)$ is also plotted. All results are shown in Fig. 1.

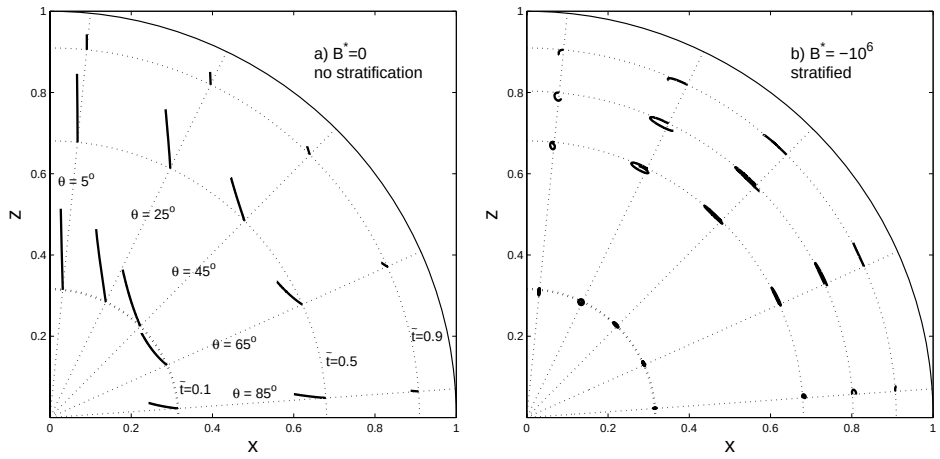

Figure 2: Trajectories within the inner core. Twenty samples are introduced at the inner core boundary at different colatitude, $\theta = 5, 25, 45, 65$ and 85 degrees, and different times, $\tilde{t} = 0.1, 0.5, 0.7$, and 0.9. *(a)* model with no stratification ($B^* = 0$), the time $\tilde{t} = 0.7$ is omitted for clarity. *(b)* model with stratification ($B^* = -10^6$).

2.4. Numerical results

2.4.1. Neutral flows, $B = 0$

The case $B = 0$ (Fig. 1) corresponds to no back reaction of the archimedean force on the flow. Yoshida et al. (1996) have derived analytically the solution and we can compare our numerical result shown in figure 1 to their analytical model. The absence of stratification allows the flow to develop into the whole inner core. Continuous relaxation of the dynamic topography results in a flow from the equator to the poles with a quadripolar pattern. The average strain rate is rather small $\dot{\epsilon} \approx 3 \times 10^{-18}$ s^{-1} ≈ 0.1 Gyr^{-1}. In other words, it takes 1 Gyr to accumulate a deformation of 10% in the material sample. The deformation induced texture is expected to be weak, as will be seen in section 3, except at the center of the inner core where strain rate can

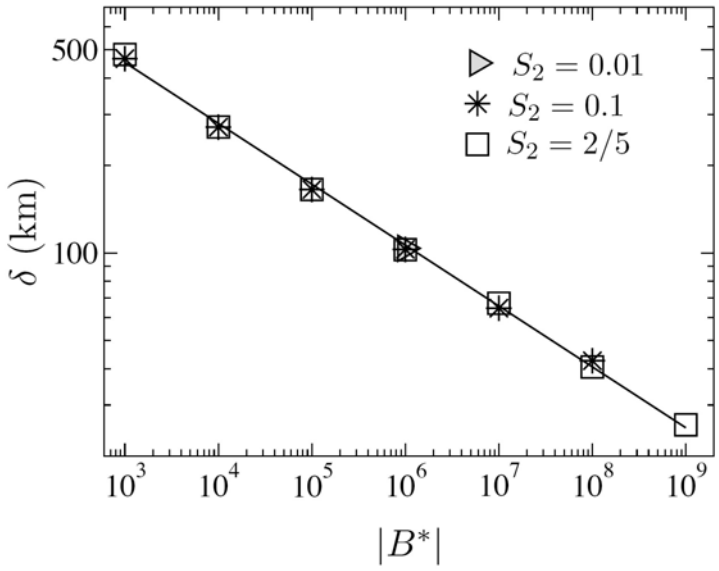

Figure 3: Evolution of the thickness δ of the uppermost stratified layer with the dimensionless buoyancy number B^* for different values of differential growth parameter S_2 (Eq. 10).

reach values of 1.5 Gyr^{-1} during the first stage of the inner core growth.

Note the strong deformation of the isoconcentration surfaces in the final stage. It shows how the spherical boundary of the inner core in the past is modified to take an axial oblate shape in the final inner core. This motion is also apprehended by the trajectories of samples set at the ICB and transported by the flow during its later evolution as shown in figure 2a.

2.4.2. Stratified flows

Calculations for a stratified flow ($B^* = -10^6$) are also presented in Fig. 1. As explained in section 2.3, the magnitude of B increases from 0 to B^* during the growth of the inner core. The effect of the stratification is negligible early in the inner core history, but becomes rapidly important as the inner core

grows and B increases. The stratification tends to prevent radial motion because deformation of isodensity surfaces induces restoring archimedean forces. As the stratification strengthens, the flow is forced to follow isodensity surfaces and becomes quasi-horizontal. The radial penetration is strongly reduced and the flow is progressively confined in a thin shear layer below the ICB, of thickness δ. An important consequence of the localization of the flow is that the magnitude of the strain rate which is associated becomes much larger, as can be seen in figure 1.

Momentum is transmitted deeper in the inner core by viscous entrainment, and the flow takes the form of a vertical series of elongated cells with vorticity of alternating sign. The specific geometry of the flow results from the competing effects of the stratification, which inhibits vertical motion, and of the symmetry of the forcing, which implies that the horizontal velocity must vanish in the equatorial plane and on the N-S axis. In the vicinity of the equatorial plane and of the N-S axis, the flow is deflected and forced to be locally vertical. Stratification limits this vertical flow which is forced to rotate further until it becomes horizontal again (the deformation of the isodensity surfaces acts as a localized source of vorticity). The thickness of the resulting cells depends on the magnitude of the local stratification. The associated strain rate vanishes quickly in depth and is mainly concentrated in between the two first shallower cells.

Figure 2b shows the trajectories of different particles introduced at the surface of the inner core at different time during its growth. The trajectories are quasi horizontal below the ICB, with a maximum of amplitude at mid latitude. Deeper within the inner core, the particles follow the return flow

associated with the viscous counter cell. At polar and equatorial latitudes, as well as in the deepest parts, the radial and horizontal displacement are equivalent and the particles follow almost circular trajectories.

2.4.3. Scaling laws for the thickness of the layers

Simulations with different values of the differential growth S_2 have been performed (shown in figure 3). The amplitude of the flow is found to be proportional to S_2 but, perhaps surprisingly, the dimensionless depth $\tilde{\delta}$ of the alternating layers does not depend on S_2 when $S_2 < 1$. Nevertheless, as shown in figure 3, the thickness of the layer varies with B and we find $\tilde{\delta} \approx 1.6|B|^{0.20\pm0.01}$ from a fit for $3 < \log|B| < 9$.

This scaling can be explained as follow. The thickness of the first cell should correspond to the depth at which the buoyancy forces resulting from the deformation of isodensity surfaces balance the viscous forces, by the mean of pressure, and prevent any further vertical motion. The uppermost cell has a dimensionless horizontal elongation equal to 1 and a dimensionless thickness $\tilde{\delta}$. From the dimensionless incompressibility equation, we can deduce that the horizontal component of the velocity in the layer $\tilde{v_\theta}$ is $O(S_2\,\tilde{\delta}^{-1})$ since the vertical component $\tilde{v_r}$ imposed by the boundary condition is of order S_2 ($S_2 u_{icb}$ in dimensional unit). The vorticity $\boldsymbol{\nabla} \times \mathbf{v}$ is then $O(S_2\,\tilde{\delta}^{-2})$. The dimensionless vorticity equation (13) writes

$$\boldsymbol{\nabla}^2 \boldsymbol{\nabla} \times \mathbf{v} = B \frac{\partial \tilde{c}}{\partial \theta} \mathbf{e}_\phi, \tag{21}$$

from which a scaling for $\tilde{\delta}$ can be derived. The scaling of $\partial\tilde{c}/\partial\theta$ can be found by considering the deformation by the flow in the upper cell of a newly cristallized, initially horizontal, isocompositional surface. This isocompo-

sitional surface is progressively tilted by the flow and, at a time $\delta\tilde{t}$ after solidification, the resulting horizontal compositional gradient is of order

$$\frac{\partial \tilde{c}}{\partial \theta} \sim \left| \frac{\partial \tilde{c}}{\partial \tilde{r}} \right| \tilde{v_r}\, \delta\tilde{t} \sim S_2\, \delta\tilde{t} \tag{22}$$

since $|\partial\tilde{c}/\partial\tilde{r}| = O(1)$ and $\tilde{v_r} = O(S_2)$. It reaches a maximum in the transition zone between the two upper cells, at a depth $\tilde{\delta}$, where vorticity changes sign. If the deformation velocity is small compared to the mean growth rate of the inner core, material crystallized at the ICB is buried to a depth $\delta\tilde{t}$ in a time $\delta\tilde{t} = \tilde{\delta}/\tilde{u_{\rm icb}} = \tilde{\delta}$. The maximum horizontal compositional gradient is then $\partial\tilde{c}/\partial\theta = O(S_2\,\tilde{\delta})$. Using this scaling in equation (21), we deduce that the thickness of the shear layer scales as

$$\tilde{\delta} \sim |B|^{-1/5}, \tag{23}$$

which has no dependence in S_2. The scaling exponent estimated above from the numerical simulations is in very good agreement with the value 1/5 predicted by the scaling analysis.

The scaling law (23) implies that the strain rate in the uppermost shear layer should scale as

$$\dot{\epsilon} \sim \frac{\tilde{u_\theta}}{\tilde{\delta}} \sim S_2\, |B|^{2/5}. \tag{24}$$

This shows that stratification is necessary to reach a large deformation in a time shorter that the age of the inner core. The 2/5 power is small but the buoyancy number can easily reach values large enough to concentrate the strain in the uppermost layer. With $B^* = -10^6$, the shear layer has a current thickness $\delta \sim 100$ km, and strain rates of 0.015 Myr^{-1} are obtained in the uppermost layer. This corresponds to a horizontal cumulative deformation of

more than 100% in a material sample during its burying below the dynamical superficial layers. Note that since B is an increasing function of time, δ decreases and $\dot{\epsilon}$ increases with time.

3. Mineralogical model

It is generally accepted that the stable phase of pure iron at inner core conditions is hexagonal close packed (*hcp*) (e.g. Mao et al., 1990; Ma et al., 2004; Dewaele et al., 2006). The presence of light elements in the core is said to stabilize cubic phases high temperature (Vočadlo et al., 2003; Dubrovinsky et al., 2007; Côté et al., 2008). Kuwayama et al. (2008) also argued that a transition from an *hcp* to an fcc phase could explain the enigmatic presence of the innermost inner core (Ishii and Dziewoński, 2002; Niu and Chen, 2008), although the range of composition at which this can occur is tight. For the sake of simplicity, in this paper, we will restrict ourself and assume that the inner core is composed of pure *hcp*-Fe.

3.1. Plastic properties

To this day, the determination of active deformation mechanisms in iron at core conditions remains an active field of research (Poirier and Price, 1999; Wenk et al., 2000; Merkel et al., 2004; Miyagi et al., 2008; Liermann et al., 2009) and more experiments will be needed to properly constrain those parameters.

At room temperature, plastic deformation in *hcp*-Fe is controlled by a dominant $(0001)\langle\overline{1}2\overline{1}0\rangle$ basal slip, with a contribution of $\{10\overline{1}0\}\langle\overline{1}2\overline{1}0\rangle$ prismatic slip, and other minor contributions (Wenk et al., 2000; Merkel et al., 2004). At higher temperature, pyramidal $\langle c{+}a\rangle$, $\{2\overline{1}\overline{1}2\}\langle 2\overline{1}\overline{1}3\rangle$ becomes more

Slip type	Plane	Direction	CRSS
Basal	(0001)	$\langle\bar{1}2\bar{1}0\rangle$	0.5
Prismatic	$\{10\bar{1}0\}$	$\langle\bar{1}2\bar{1}0\rangle$	1.0
Pyramidal $\langle a\rangle$	$\{10\bar{1}1\}$	$\langle\bar{1}2\bar{1}0\rangle$	3.0
Pyramidal $\langle c+a\rangle$	$\{2\overline{11}2\}$	$<2\overline{11}3>$	2.0

Table 2: Slip systems and their critical resolved shear stress (CRSS) of *hcp*-Fe used in our simulations.

dominant (Miyagi et al., 2008) and allows an easier rotation of the Fe grains. In agreement with those experimental results, we assume easy basal slip and allow significant contribution of prismatic and pyramidal $\langle c+a\rangle$ slip (Table 2).

LPO in Fe polycrystals were simulated using the Los Alamos viscoplastic self-consistent (VPSC) code of Lebensohn and Tome (1993). The VPSC model treats each grain as an inclusion in a homogeneous but anisotropic medium that has the average properties of the polycrystal. It is intermediate between the Taylor model that enforces strain compatibility and the Sachs model that is based on stress equilibrium. One to one grain interaction or intergranular heterogeneities are not accounted for directly, but using a mean field approach. As deformation proceeds, crystals deform and rotate to generate preferred orientation. By applying different critical resolved shear stresses (CRSS) to slip systems and twin modes, the model will favor one deformation mode over another. It was already used for inner core modeling by Wenk et al. (2000) and Buffett and Wenk (2001) and has been reliable for simulating textures of many low symmetry materials (Wenk, 1999).

For each deformation step, we extracted the velocity gradients for markers

placed inside our inner core formation models. Those gradients are then used as inputs for simulating texture evolution of a 3000 grains Fe aggregate using VPSC. Orientations in the aggregates are characterized by an orientation distribution functions (ODF). The ODF is a probability function for finding an orientation and it is normalized over the whole orientation space to unity. An aggregate with a random distribution function has a probability of one for all orientations, or one multiple of a random distribution (m.r.d.). If preferred orientation is present, some orientations have probabilities higher than one and others lower than one but orientation probabilities can never be less than zero. Three dimensional ODF are not easy to visualize. Here, we will display pole figures of the $\langle a \rangle$ and $\langle c \rangle$ directions. In order to match the meridional representation of the flow, we place the z-direction (axis of rotation of the Earth) at the top of the figure, the x-axis (cylindrical radial direction) at the right of the figure, and the y-axis (azimuthal direction) at the center.

3.2. Initial texture

Simulations were run with both a random initial texture and a pretexture due to solidification. It seems quite likely that a texture can be frozen-in at the ICB during solidification (Bergman, 1997; Brito et al., 2002), in particular if the inner core grows dendriticaly, as predicted by theoretical analysis (Fearn et al., 1981; Shimizu et al., 2005; Deguen et al., 2007). Dendritic crystallization of *hcp* materials typically leads to cristallographic preferred orientation with the basal planes of the crystals parallel to the gradient of temperature (*e.g.* Bergman et al., 2000, 2003). Therefore, pretexture due to solidification at the ICB was represented by an ODF with the majority of

the $\langle c \rangle$ axis in the horizontal plane and the $\langle a \rangle$ axis perpendicular to the ICB (Fig. 4).

3.3. Time evolution of texturing

Figure 5 shows an example of outputs of the dynamical model assuming stratified flow ($B^* = -10^6$), for a polycrystalline aggregate introduced at time $\tilde{t} = 0.5$, colatitude $\theta = 45°$, and radius 0.96. Our calculations assume an incompressible fluid and thus $\sum_i \dot{\epsilon}_{ii} = 0$. For this particular tracer, deformation is dominated by the xx and zz components of the deformation tensor with $\dot{\epsilon}_{xx} \approx -\dot{\epsilon}_{zz}$. This corresponds to simple shear applied at 45° with respect to the Earth reference frame, in the direction of flow (Fig. 5).

The rigid body rotation of the aggregate is given by ω_y. This component is important in magnitude and induces a rotation of aggregate around the azimuthal axis that affects the texture in the material.

Corresponding textures simulated for an *hcp*-Fe aggregates are shown in Fig. 6 assuming crystallization textures of Fig. 4. Texture develops very quickly as the aggregate is in the top layer and migrates toward the pole. At time $\tilde{t} = 0.6$, texture is fully developed, with the a and c-axes of the aggregate mainly distributed along the North-South and East-West directions, respectively.

4. Evolution of lattice preferred orientation during inner core growth

4.1. Neutral flow, B=0

In this case, we do not account for stratification, and flow can develop into the whole inner core (section 2.4.1, Fig. 2a). At the very center of the

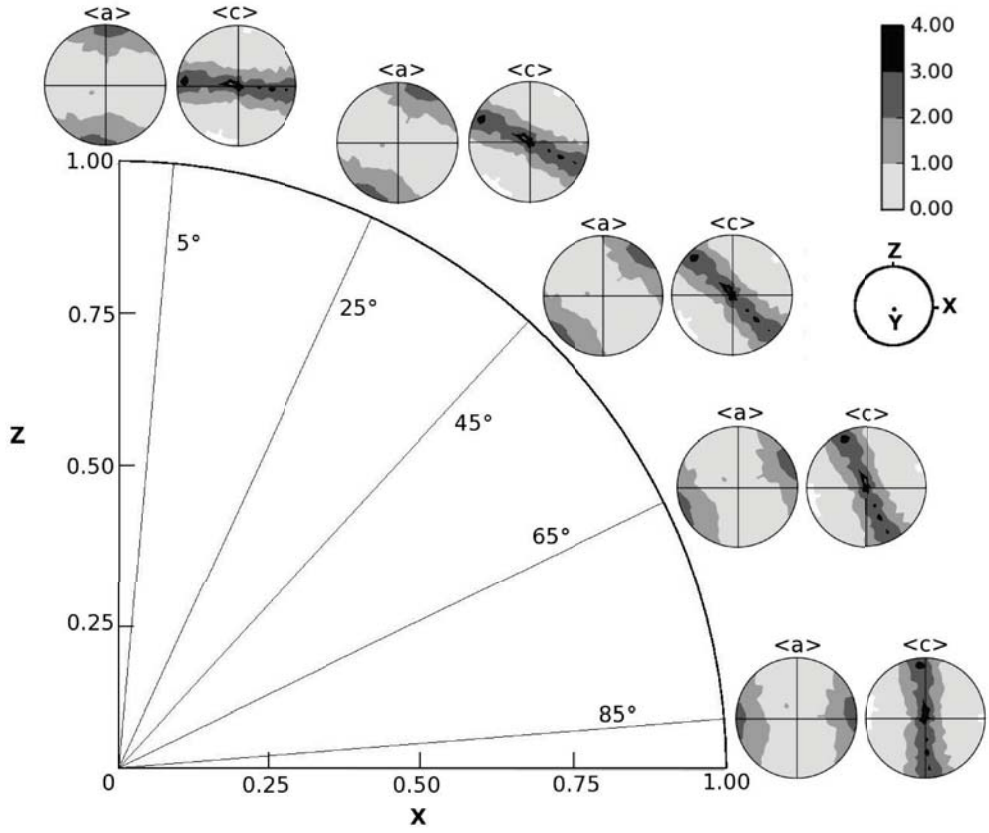

Figure 4: Pretexture due to solidification at the ICB, expressed using pole figures of the $\langle a \rangle$ and $\langle c \rangle$ directions, for colatitudes of 5, 25, 45, 65, and 85°. Linear scale, equal-area projection, contours in multiples of a random distribution (m.r.d.). Maximum intensity of the $\langle a \rangle$ and $\langle c \rangle$ pole figures are 3.1 and 4.3 m.r.d., respectively.

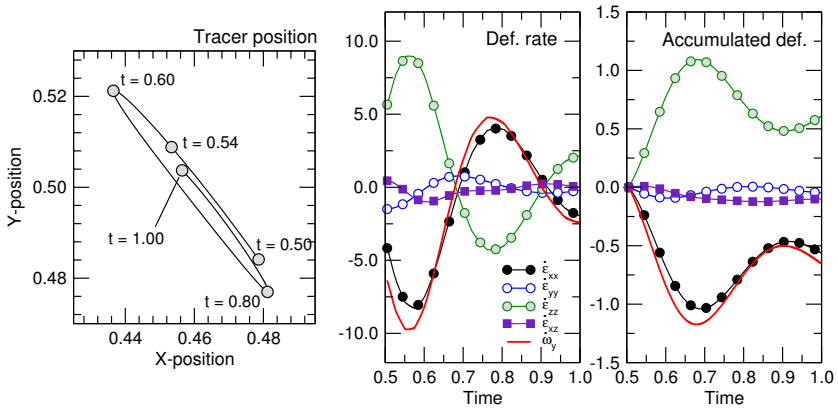

Figure 5: Trajectory, components of the strain rate tensor ($\dot{\epsilon}_{xx}$, $\dot{\epsilon}_{yy}$, $\dot{\epsilon}_{zz}$, $\dot{\epsilon}_{xy}$), rigid body rotation ($\dot{\omega}_y$), and accumulated deformation (ϵ_{xx}, ϵ_{yy}, ϵ_{zz}, ϵ_{xy}) and rotation (ω_y) vs. time for a particule introduced at time $\tilde{t} = 0.5$, colatitude 45°, and radius 0.96.

inner core, plastic deformation is large enough to modify the orientation of the aggregates at the beginning of the inner core formation. Later on, and consequently further out in the inner core, deformation becomes weaker and is not sufficient to induce any texture development.

With a random crystallization texture, strong LPO concentrate at the center of the inner core (Fig. 7, aggregates introduced at $\tilde{t} = 0.1$). The inner core itself could be seen as a sample in a pure shear deformation with a compression in the equatorial plane and an extension along the polar axis. This explains why the samples crystallized at $\tilde{t} = 0.1$ all show the same LPO. The distribution of c-axis shows a pronounced maximum 10° to 15° away from the equatorial plane while a axis concentrate toward the poles and a secondary maximum at colatitudes of 60°. The 10° to 15° deviation of c-axis from the equatorial plane may be surprising at first, but can be related to deformation experiments on hcp-Fe as well as numerical modeling of com-

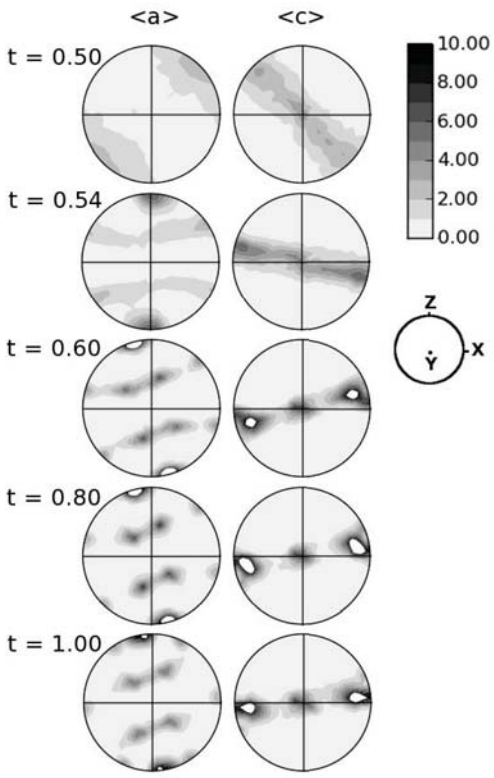

Figure 6: Pole figures of the $\langle a \rangle$ and $\langle c \rangle$ directions illustrating the LPO simulated for an *hcp*-Fe aggregate introduced in the inner core time $\tilde{t} = 0.5$, colatitude 45°, and radius 0.96 (Fig. 5), assuming a crystallization texture as in Fig. 4. Grey scale in m.r.d.

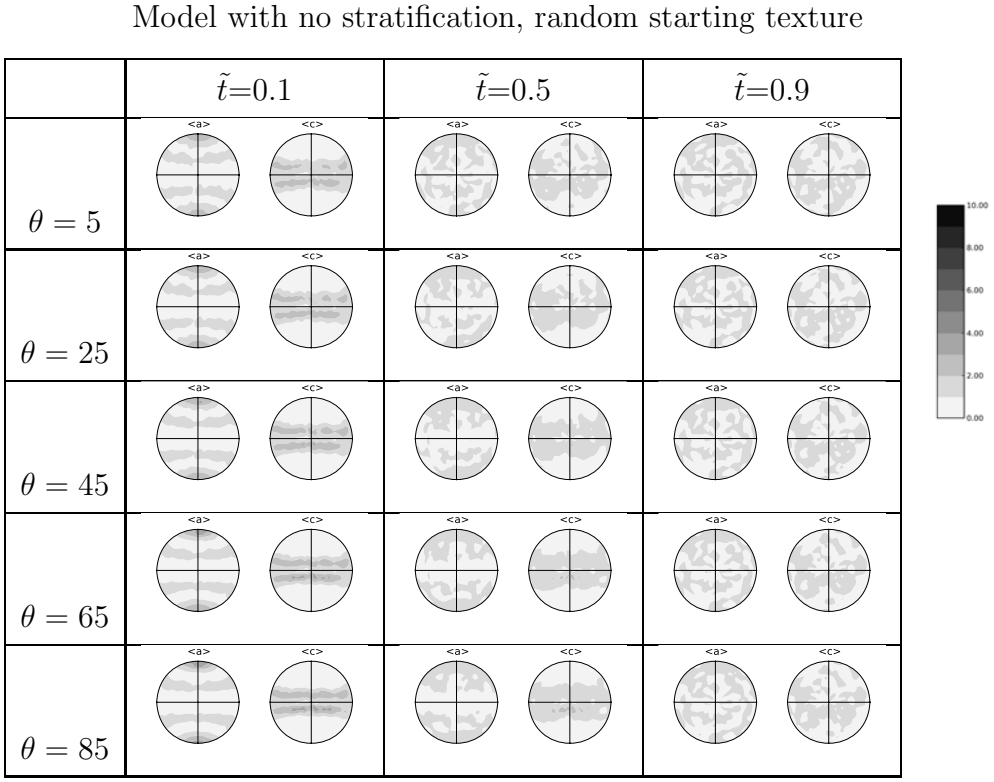

Figure 7: Pole figures of the $\langle a \rangle$ and $\langle c \rangle$ directions representing present day LPO in hcp-Fe aggregates introduced at colatitudes $\theta = 5, 25, 45, 65$ and 85° and times, $\tilde{t} = 0.1, 0.5$, and 0.9. Inner core growth model with no stratification and assuming random texture after crystallization. Corresponding trajectories can be seen in Fig. 2a. Linear scale, equal-area projection, contours in multiples of a random distribution (m.r.d.), axis as in figure 6.

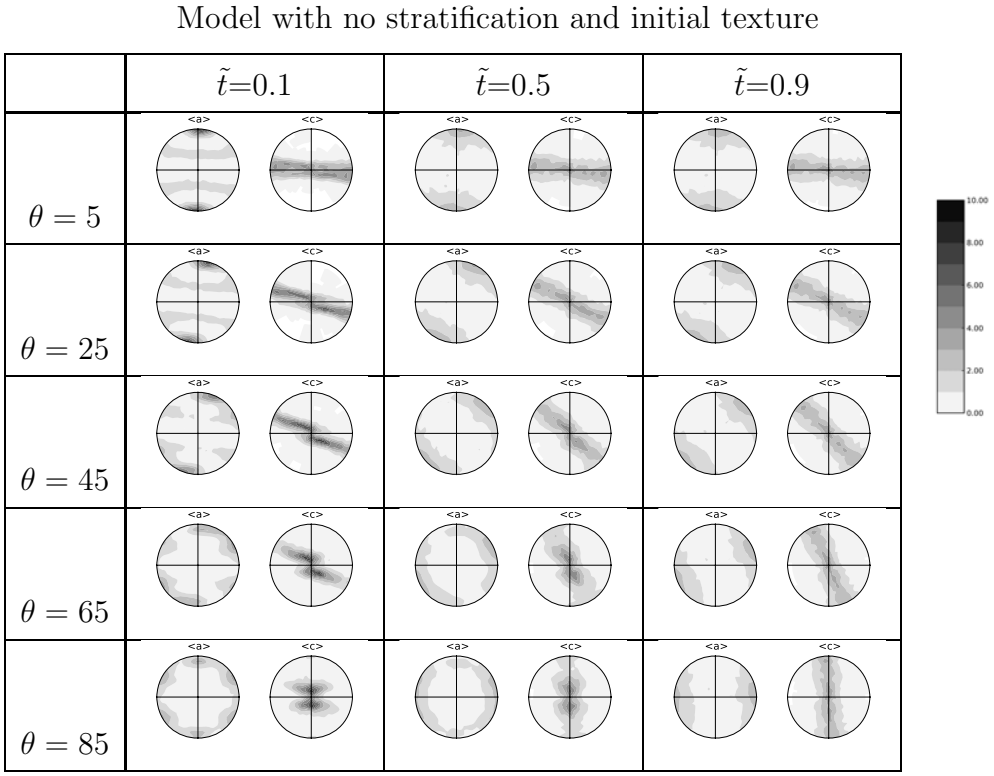

Figure 8: Pole figures of the $\langle a \rangle$ and $\langle c \rangle$ directions representing present day LPO in hcp-Fe aggregates introduced at colatitudes $\theta = 5, 25, 45, 65$ and $85°$ and times, $\tilde{t} = 0.1, 0.5$, and 0.9. Inner core growth model with no stratification and assuming crystallization textures as in Fig. 4. Corresponding trajectories can be seen in Fig. 2a. Linear scale, equal-area projection, contours in multiples of a random distribution (m.r.d.), axis as in figure 6.

pression experiments (Merkel et al., 2004) in which compressions textures do not align exactly with 0001 but are shifted 10° to 15° away from it.

If one assumes an initial crystallization texture as in Fig. 4, a long time is necessary for the textures to be affected by the flow, as can be seen in Fig. 8. Only aggregates in the central portion of the inner core (introduced at $\tilde{t} = 0.1$ and $\tilde{t} = 0.5$ in Fig. 8) are significantly affected by the deformation. Aggregates in the outer section of the core (introduced at $\tilde{t} = 0.9$ in Fig. 8) preserve their crystallization texture. Close to the axis of rotation, the plastic deformation is compatible with the pretexturing and reinforce the alignment of the a-axis with the geographic axis (e.g. $\tilde{t} = 0.1$, $\theta = 5°$). In the equatorial region (e.g. $\tilde{t}$=0.1, $\theta = 85°$), the c-axis originally aligned nearly perpendicular to the z axis tend to move perpendicular to the meridional plane, inducing an hexagonal distribution of the a-axis in the meridional plane. This is a signature of the hexagonal structure of the crystal and its sliding planes.

4.2. Stratified flow, $B = -10^6$

For a stratified flow, and assuming random crystallization textures, aggregates tend to develop strong textures in the outer layers of the core (Fig. 9) where maximum plastic deformation is attained (Fig. 1). Near the center ($r < 0.5$, aggregates introduced at $\tilde{t} = 0.1$), textures are weak and the signature of plastic deformation can not be detected. This can be attributed to the very moderate buoyancy number and the small corresponding strain rate (24) at the beginning of inner core formation. Later in the history of the inner core, the buoyancy number increases and the material acquires LPO by simple shear in the very thin superficial layer in a relatively short time scale.

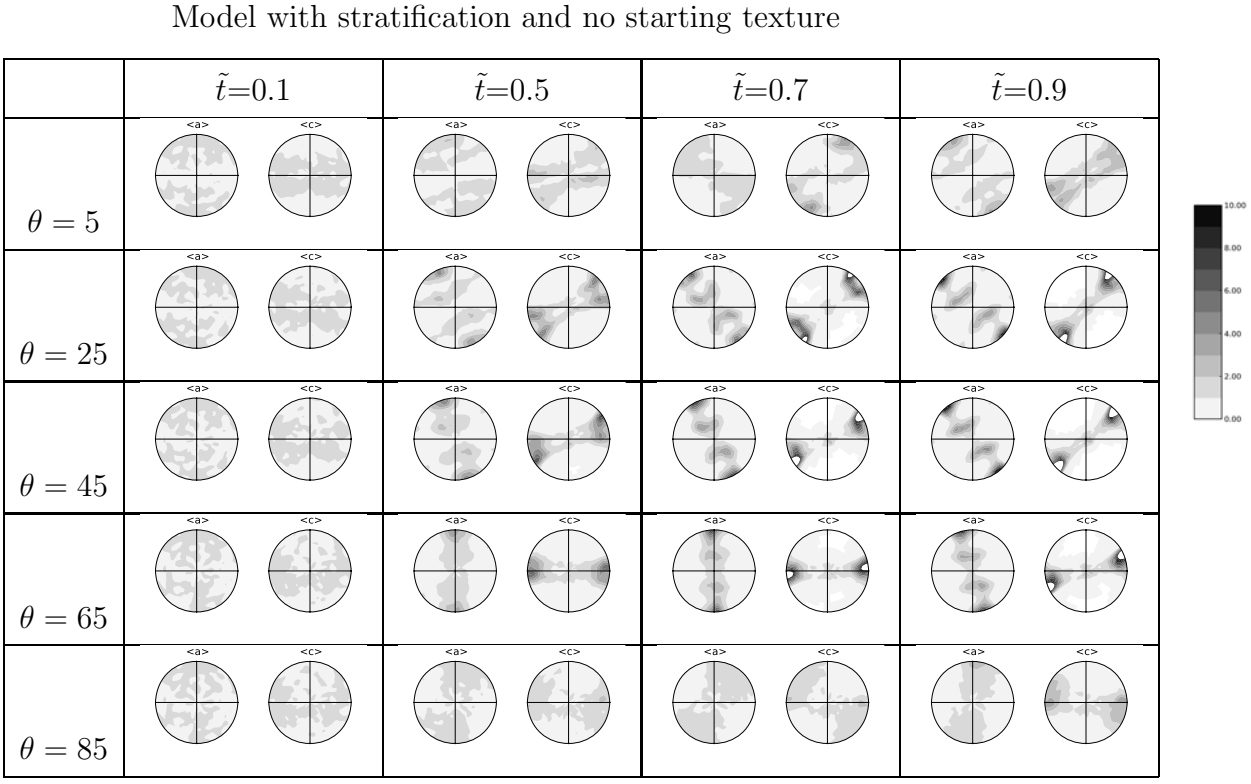

Figure 9: Pole figures of the $\langle a \rangle$ and $\langle c \rangle$ directions representing present day LPO in hcp-Fe aggregates introduced at colatitudes $\theta = 5, 25, 45, 65$ and $85°$ and times, $\tilde{t} = 0.1, 0.5, 0.7,$ and 0.9. Inner core growth model with with stratification $B = -10^6$ and assuming random starting textures. Corresponding trajectories can be seen in Fig. 2b.Linear scale, equal-area projection, contours in multiples of a random distribution (m.r.d.), axis as in figure 6.

Model with stratification and an initial texture

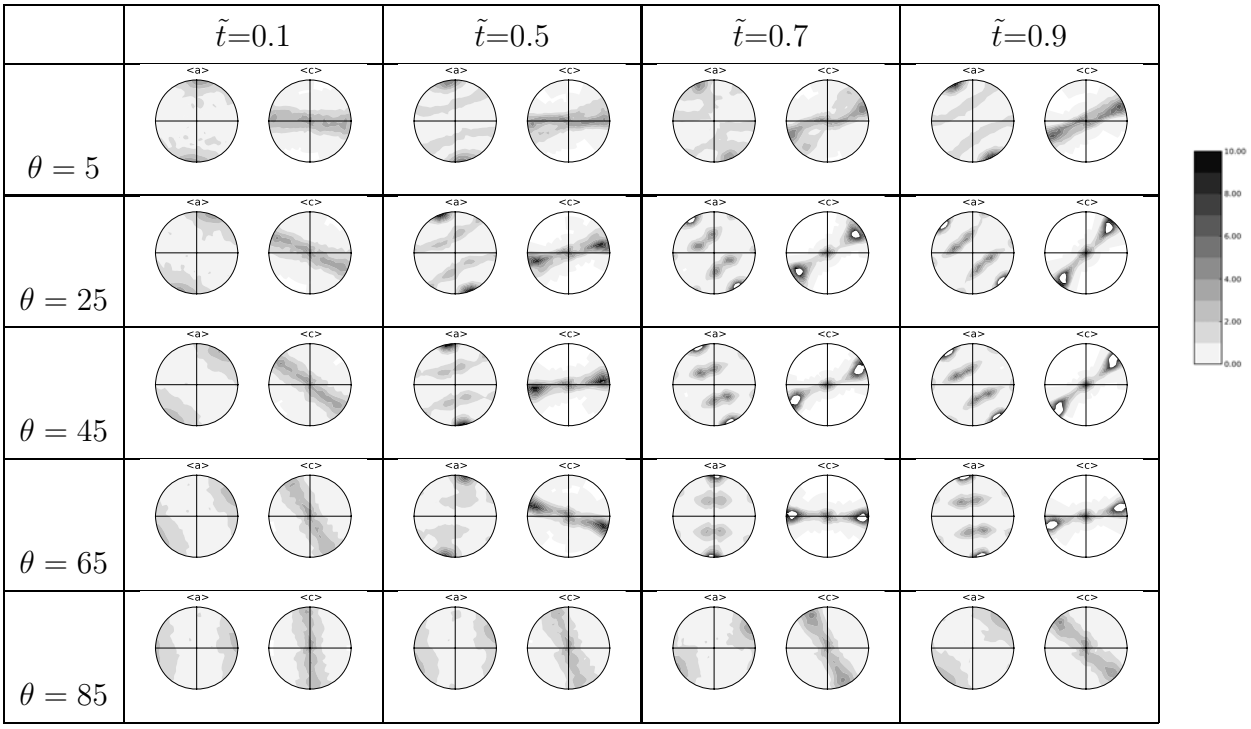

Figure 10: Pole figures of the $\langle a \rangle$ and $\langle c \rangle$ directions representing present day LPO in hcp-Fe aggregates introduced at colatitudes $\theta = 5, 25, 45, 65$ and 85° and times, $\tilde{t} = 0.1, 0.5, 0.7$, and 0.9. Inner core growth model with with stratification $B = -10^6$ and assuming crystallization textures as in Fig. 4. Corresponding trajectories can be seen in Fig. 2b. Linear scale, equal-area projection, contours in multiples of a random distribution (m.r.d.), axis as in figure 6.

In the uppermost shear layer, at mid latitude, the c-axis tends to orientate along the radial direction (the local vertical), perpendicular to the shear plane. The a-axis are mainly in the local horizontal plane with a primary orientation in the direction of the shear and a secondary direction at 60° off the meridional plane. In deeper portions of the core, rigid body rotation and simple shear change these orientations but by less than 20°.

In the equatorial disk and the polar cone, Fe aggregates exhibit a weak texture: the vertical migration of material in these region is associated with pure shear but is much smaller. The pure shear deformation would tend to align the c-axis with the major compression direction, and a-axis in the extension direction. From the scaling laws deduced in section 2.4.3, we can show that the deformation associated with the pure shear is a factor $\tilde{\delta}$ smaller than the simple shear at mid latitude. In those two regions, rigid body rotation of the aggregates plays an important role and rotates the deformation texture around the y-axis (clockwise in the equatorial disk and the opposite and the polar region).

In summary, for a stratified inner core, large texturing is produced mainly in the thin outer layer at mid latitude and is preserved for $r > 0.5$.

Assuming initial crystallization texture as in Fig. 4, the starting texture is preserved in the central portion of the core (Fig. 10, aggregates introduced at $\tilde{t} = 0.1$). Along the axis of rotation (Fig. 10, $\theta = 5°$) and the equatorial plane (Fig. 10, $\theta = 85°$), the solidification texture is rotated by the rigid body rotation of the sample, as shown in Fig. 2b. In the superficial shear layer, the texture is heavily transformed to textures resembling that of the Fig. 9, when a random crystallization texture was assumed.

5. Predicted anisotropy of the inner core

5.1. Elastic properties of hcp-Fe at inner core conditions

Calculation of seismic wave velocities inside crystal aggregates requires the knowledge of single crystal elastic moduli. The elastic properties of iron are difficult to evaluate experimentally at inner core conditions (e.g. Mao et al., 1998; Fiquet et al., 2001; Merkel et al., 2005; Antonangeli et al., 2006; Badro et al., 2007; Mao et al., 2008) while they remain a challenge for the most advanced *first principles* calculations (e.g. Stixrude and Cohen, 1995; Laio et al., 2000; Steinle-Neumann et al., 2001; Gannarelli et al., 2003, 2005; Vočadlo et al., 2009; Sha and Cohen, 2010). From those experiments and calculations, the anisotropy of *hcp* iron remains unclear. Low temperature, high pressure calculations (Stixrude and Cohen, 1995; Laio et al., 2000; Steinle-Neumann et al., 2001; Gannarelli et al., 2003, 2005; Vočadlo et al., 2009; Sha and Cohen, 2010) suggest that P-wave propagation is faster along the c-axis than along the a-axis, in agreement with low pressure/low temperature *hcp* analogs. Experimental determination of the elastic constants suggest a fast direction lying at an intermediate angle between the a and c-axis (Mao et al., 1998; Merkel et al., 2005), but the technique that was used includes serious artifacts related to stress heterogeneities induced by plastic deformation (Antonangeli et al., 2006; Merkel et al., 2009). At inner core pressures and temperatures, Steinle-Neumann et al. (2001) found a reversal of anisotropy, with the a-axis faster than the c-axis but the validity of their calculation has been questioned (Gannarelli et al., 2003, 2005). Yet recent *ab initio* calculations at inner core pressure and temperature by Vočadlo et al. (2009) and Sha and Cohen (2010) again suggest that anisotropy in iron changes at high tem-

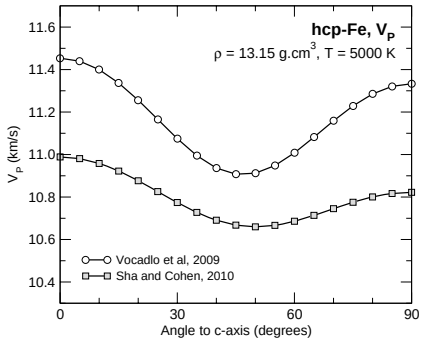

Figure 11: P-wave velocity in hcp-iron at 5000 K and core density according to the *ab initio* calculations of Vočadlo et al. (2009) and Sha and Cohen (2010) as a function of propagation direction with respect to the c-axis. Results of Sha and Cohen (2010) have been interpolated to a density of $\rho = 13.15$ g.cm^{-3} and temperature $T = 5000$ K.

perature. Results of the two calculations differ, both for the average P-wave velocity and the amplitude of anisotropy (Table 3 and Fig. 11). However, both calculations find that P-waves travel faster along the c than the a axis, with a pronounced minimum 45° away from c. Here, we will use the set of elastic moduli of Vočadlo et al. (2009). Calculations using the elastic moduli of Sha and Cohen (2010) would not change the style of anisotropy, but only the absolute P-waves velocities and the amplitude of anisotropy.

5.2. Model with no stratification and a random crystallization texture

Figures 12a shows the present day P wave velocities inside the inner core obtained for a growth model with no stratification and assuming a random crystallization texture. In the central portion, P wave velocity is faster along the NS axis than any equatorial or mid latitude direction. In the outer portions of the core, anisotropy is weak.

As in Yoshida et al. (1996), the orientation of anisotropy has a cylindrical

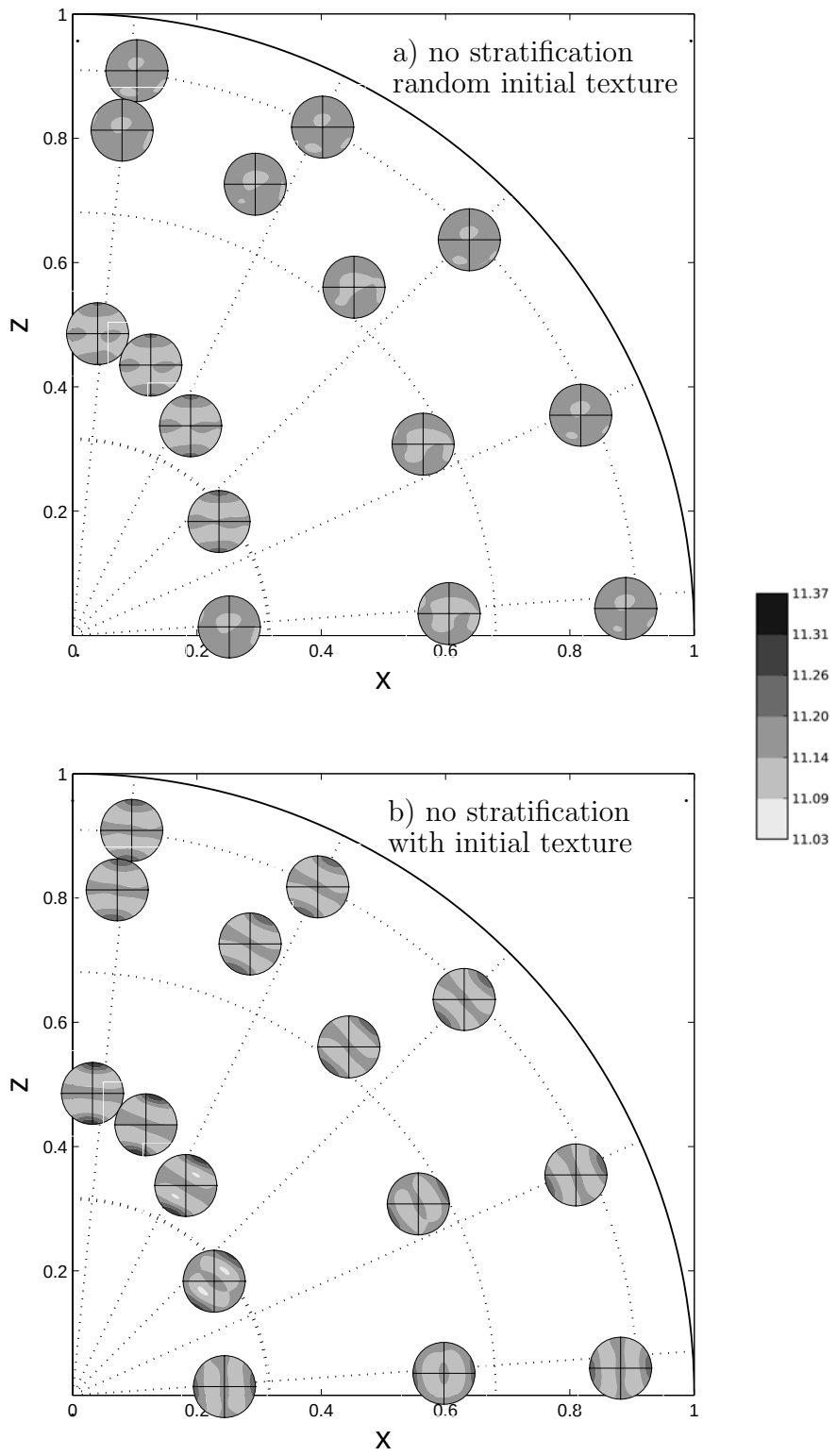

Figure 12: Present day P wave velocity anisotropy inside the inner core for a model with no stratification ($B = 0$). *(a)* Model with a random solidification texture, corresponding to the hcp-Fe textures of Fig. 7. *(b)* Model with initial solidification texture, corresponding to the hcp-Fe textures of Fig. 8. Velocity scale are in km/s. Each contour corresponds to a 0.5% change in velocity.

	Vočadlo *et al* (2009)	Sha and Cohen (2010)
c_{11}	1689	1540
c_{33}	1725	1588
c_{12}	1186	1019
c_{23}	990	920
c_{44}	216	254
ρ	13.154 g.m^{-3}	13.15 g.cm^{-3}

Table 3: Interpolated isothermal elastic constants (in GPa) for hcp-Fe at 5000 K. $c_{66} = (c_{11} - c_{12})/2$

symmetry with the fastest direction along the N-S axis, in agreement with seismological observations, but the predicted amplitude of anisotropy is significantly weaker than observed. At most, the P-wave velocity is 1% faster along the NS axis in the very central part ($r < 0.5$). As such, global travel time anisotropy would be significantly less than 1%. This is far from the 3% anomaly observed by seismologists (Souriau, 2003). In addition, the slowest direction in this model is at about 45° from the N-S axis.

Under our assumptions (equatorial growth model, plastic model, and hcp-Fe elastic properties), this simple model has three major weaknesses:

(i) The direction of anisotropy is correctly predicted, but the cumulated deformation is not sufficient to generate the observed inner core anisotropy.

(ii) Seismological observations indicate that the uppermost inner core has distinct seismological properties. This model does not generate any specific superficial layer at the top of the inner core.

(iii) This model requires that the axis of rotation of the inner core did not

significantly wobble during the time life of the inner core.

5.3. Model with no stratification and a non-random crystallization texture

Solidification texturing can produce strong anomalies at the top of the inner core. In this model, directional variations of P-wave velocities can be seen throughout the core, with anisotropy amplitudes reaching about 1.5% (Fig. 12b). In most of the core, the calculated fast direction of propagation is mostly radial, with a secondary maximum in the plane perpendicular to the radial direction. This configuration poorly explains the seismological data as ray paths integrations would not show a strong variation of travel time with the ray angle.

5.4. Model with stratification and a random crystallization texture

Stratification inhibits radial flows, concentrates the deformation in a superficial horizontal layer and produces important simple shear that can generate strong LPO and large seismic anisotropy. Figure 13a shows the present day P-wave velocity distribution inside the inner core for a model with moderate stratification and assuming a random crystallization texture.

The amplitude of anisotropy is large (3%) but is mostly localized in the outer portion of the inner core, away from the equator and the pole. The directions of fast propagation are mainly oriented along the direction of shear, horizontal relative to ICB, with a slight rotation as the material plunges deeper into the core. This rotations induces a shift of fast direction of propagation from the local horizontal towards a North South direction (e.g. $r \approx 0.7$). Note the quadrangular shape of the anisotropy figure which

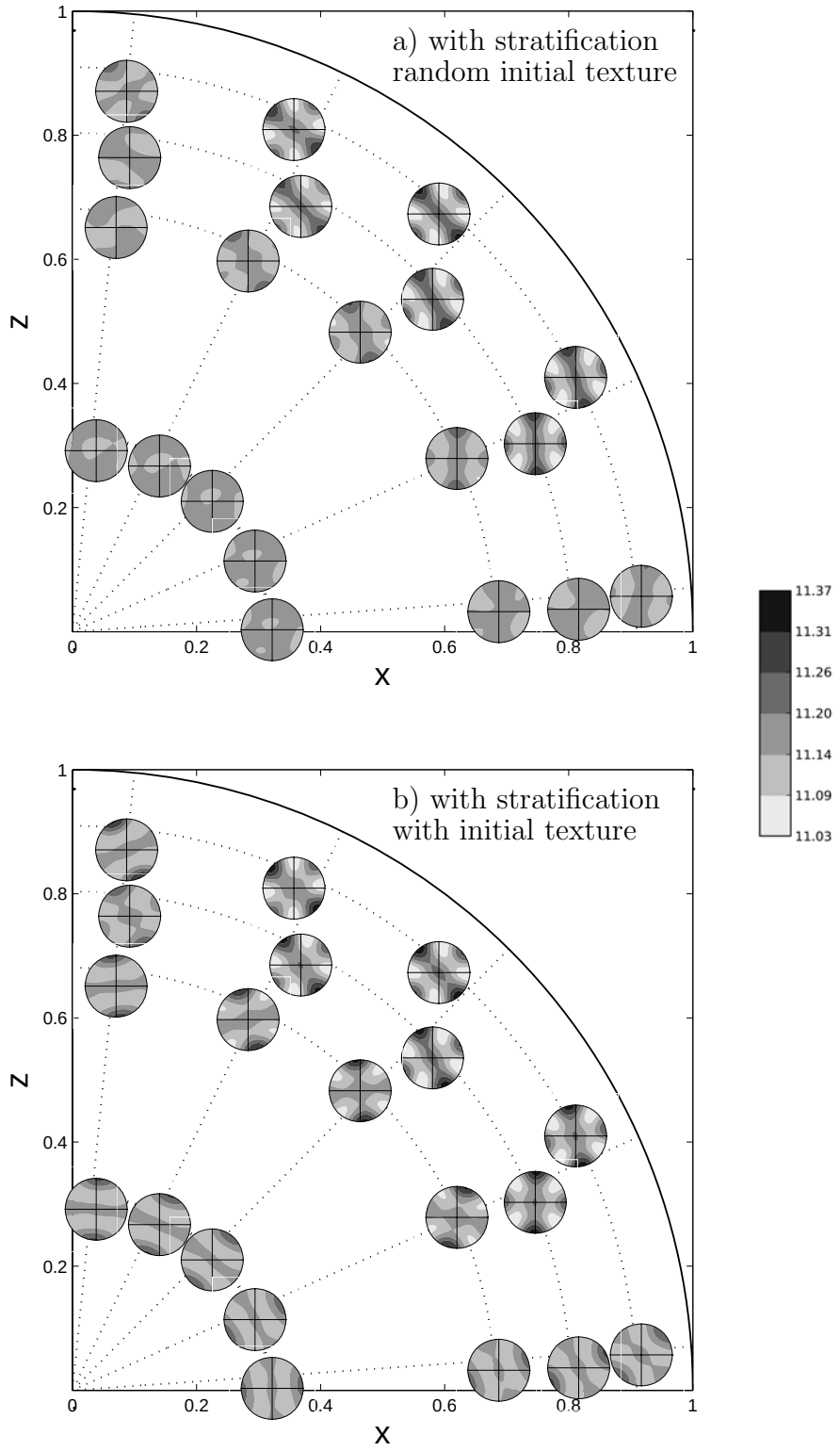

Figure 13: Present day P wave velocity anisotropy inside the inner core for a model with stratification ($B = -10^6$). *(a)* Model with a random solidification texture, corresponding to the hcp-Fe textures of Fig. 7. *(b)* Model with initial solidification texture, corresponding to the hcp-Fe textures of Fig. 8. Velocity scale are in km/s. Each contour corresponds to a 0.5% change in velocity.

is the reminiscence of the P wave velocity minimum at 45° away from a and c in the single crystal (Fig. 11).

In the center ($r < 0.5$), anisotropy is weak. Lack of stratification early in the inner core history and stratification in the later stages of core formation inhibit deformation, therefore LPO, in this region. This lack of anisotropy in the deep inner core is in strong contradiction with seismic observations.

5.5. Model with stratification and a non-random crystallization texture

As in the previous model, there is large anisotropy is the outside portion of the inner core, away from the equator and the pole (Fig. 13b). In these region, the crystallization texture is erased and the observed anisotropy is the result of the large shear flow induced by stratification. Below $r < 0.5$, LPO associated with the solidification process are preserved. Along the equator and the N-S axis, the anisotropy induced by solidification is slightly rotated. Indeed, in those regions, aggregate are submitted to significant rigid-body rotation, but little plastic deformation (e.g. Fig.2).

The strong radial anisotropy in the uppermost layer would be difficult to detect in seismology. N-S and E-W velocities are equivalent. Moreover, it would be difficult to compare horizontal and radial traveltimes in a superficial layer ~ 100 km thick. Indeed, most studies of the uppermost inner core are based on comparison of almost horizontal rays with different orientations and would not capture our predicted anisotropy. As such our model is not inconsistent with observations of isotropy in the uppermost inner core.

Textures in the outermost inner core are a result of intense plastic deformation, and this process is fast (less than 10 Myr). In contrast, anisotropies in the deep inner core, along the equator or the N-S axis, are mostly fossil

and would therefore be very sensitive to wobbles of the inner core.

6. Conclusion

A fundamental question regarding the inner core dynamics remains whether it is stably stratified or not. Because of the large uncertainties on the age of the inner core and on most of thermo-physical parameters of the core, and on most of thermo-physical parameters of the core, in particular on the thermal conductivity, it is currently unknown whether the inner core has a stable or unstable density stratification. If the inner core is unstably stratified, convection can take the form of a 'convective translation' (Alboussière et al., 2010; Monnereau et al., 2010) if the viscosity is larger than $\sim 10^{18}$ Pa.s (Alboussière et al., 2010). If the viscosity is smaller, it would be a more classical plume regime (Weber and Machetel, 1992; Deguen and Cardin, 2011) .

Here, we assumed that the inner core is stably stratified. Stratification prevents any strong vertical motions within the inner core and forces the flow to be as horizontal as possible. The flow induced by aspherical growth of the inner core is localized in a thin shear layer below the ICB, where the strain is potentially large enough to produce a significant texture.

We successfully coupled our model of inner core dynamics with a visco-plastic deformation model to compute LPO of hcp-Fe in the inner core and predict the resulting seismological anisotropy. We emphasize on the fact, that although the procedure we developed is quite general, the exact result is function of a number of assumptions regarding the thermo-chemical state of the inner core, the stable phase of iron at inner core condition, its rheology, and its elastic properties. The choices we have made are consistent

with current beliefs and the most recent experimental and numerical studies, but there is still no consensus on these questions. It will be important to test the sensitivity of our results to the mineralogical assumptions of the model. Other possible phases of Fe, different slip systems or different elastic properties may lead to different results and deserve more numerical and experimental studies.

We summarize the principal results of texture calculations.

(i) Without stratification ($B^* \to 0$, large viscosity and small stratification):

- The degree of deformation-induced LPO increases with depth. Without solidification texturing, the outer part of the inner core is isotropic and the central region exhibits a cylindrical anisotropy.
- Deformation texturing seems too weak however to explain a $\sim 3\%$ anisotropy.
- In addition, since the texturing timescale is comparable to the age of the inner core, the development of the deep anisotropy requires that there have been no significant inner core polar wander.
- Solidification textures, if present, are only weakly reworked by subsequent deformation. The final structure of the inner core would therefore reflect the initial geometry of the solidification texture. With the solidification texture assumed here, the final texture would be spherically symmetric, in obvious disagreement with the seismological observations. Solidification texturing might explain the cylindrical anisotropy of the inner core only if, as proposed by Bergman (1997), the initial texture exhibits a N-S cylindrical symmetry due to anisotropic heat

flow in the outer core.

(ii) With a stable stratification :

- Plastic deformation in the shear layer can erase a solidification texture, and produce a strong deformation texture and seismic anisotropy at mid latitudes.
- The resulting texture in the outer part of the inner core has a spherical symmetry, and is therefore not able to explain the global cylindrical anisotropy of the inner core.
- This layer would appear isotropic to body wave seismology, but might be detectable in normal mode data.
- In this model, it is possible to produce a layered inner core, with a deep fossil texture inherited from solidification texturing, and a deformation texture in the outer part of the inner core. The relative thickness of the two layers depend on the value of the buoyancy number B^*. A larger value of B^* would result in a smaller region of fossilized solidification texture. As in the case with no stratification, the deep inner core would have a cylindrical anisotropy only if the initial solidification texture has a N-S cylindrical symmetry (Bergman, 1997).

This last model seems to be the most compatible with the seismological data.

Hemispherical seismic variations (Tanaka and Hamaguchi, 1997; Garcia and Souriau, 2000; Deuss et al., 2010) should also be studied with non axisymmetric models of inner core growth as suggested by the experiments of Sumita and Olson (1999, 2002) and the numerical simulations of Aubert et al.

(2008).

Acknowledgments. All computations presented here were performed at the Service Commun de Calcul Intensif de l'Observatoire de Grenoble. We thank the undergraduate students Jonathan Serafini and Charlotte Regnier who participated to the study. R. Deguen was partly supported by NSF grant EAR#0909622. S.Merkel was supported by ANR program DiUP, N. ANR-07-JCJC-0136. The study was granted by the program SEDIT of INSU/CNRS.

References

Albarède, F., 1996. Introduction to geochemical modeling. Cambdridge University Press, Cambridge UK.

Alboussière, T., Deguen, R., Melzani, M., 2010. Melting induced stratification above the Earth's inner core due to convective translation. Nature 466, 744–747.

Alfè, D., Gillan, M. J., Price, G. D., Apr. 2002. Ab initio chemical potentials of solid and liquid solutions and the chemistry of the Earth's core. J. Chem. Phys.116, 7127–7136.

Allègre, C. J., Poirier, J.-P., Humler, E., Hofmann, A. W., 1995. The chemical composition of the Earth. Earth and Planetary Science Letters 134, 515–526.

759 Antonangeli, D., Merkel, S., Farber, D. L., Dec. 2006. Elastic anisotropy in
760 hcp metals at high pressure and the sound wave anisotropy of the Earth's
761 inner core. Geophys. Res. Lett. 33, 24303–+.

762 Aubert, J., Amit, H., Hulot, G., Olson, P., Aug. 2008. Thermochemical flows
763 couple the Earth's inner core growth to mantle heterogeneity. Nature 454,
764 758–761.

765 Aurnou, J., Heimpel, M., Allen, L., King, E., Wicht, J., Jun. 2008. Convec-
766 tive heat transfer and the pattern of thermal emission on the gas giants.
767 Geophysical Journal International 173, 793–801.

768 Badro, J., Fiquet, G., Guyot, F., Gregoryanz, E., Occelli, F., Antonangeli,
769 D., D'Astuto, M., Feb. 2007. Effect of light elements on the sound velocities
770 in solid iron: Implications for the composition of Earth's core. Earth and
771 Planetary Science Letters 254, 233–238.

772 Bergman, M. I., 1997. Measurements of elastic anisotropy due to solidification
773 texturing and the implications for the Earth's inner core. Nature 389, 60–
774 63.

775 Bergman, M. I., Agrawal, S., Carter, M., M., M.-S., 2003. Transverse solidi-
776 fication textures in hexagonal close-packed alloys. J. Crystal Growth 255,
777 204–211.

778 Bergman, M. I., Giersch, L., Hinczewski, M., Izzo, V., Jan. 2000. Elastic and
779 attenuation anisotropy in directionally solidified (hcp) zinc, and the seismic
780 anisotropy in the Earth's inner core. Physics of the Earth and Planetary
781 Interiors 117, 139–151.

Brito, D., Elbert, D., Olson, P., Feb. 2002. Experimental crystallization of gallium: ultrasonic measurements of elastic anisotropy and implications for the inner core. Physics of the Earth and Planetary Interiors 129, 325–346.

Buffett, B. A., Aug. 1997. Geodynamic estimates of the viscosity of the Earth's inner core. Nature 388, 571–573.

Buffett, B. A., Nov. 2009. Onset and orientation of convection in the inner core. Geophysical Journal International 179, 711–719.

Buffett, B. A., Bloxham, J., Dec. 2000. Deformation of Earth's inner core by electromagnetic forces. Geophys. Res. Lett.27, 4001–4004.

Buffett, B. A., Garnero, E. J., Jeanloz, R., Nov. 2000. Sediments at the Top of Earth's Core. Science 290, 1338–1342.

Buffett, B. A., Wenk, H.-R., Sep. 2001. Texturing of the Earth's inner core by Maxwell stresses. Nature 413, 60–63.

Busse, F. H., 1970. Thermal instabilities in rapidly rotating systems. Journal of Fluid Mechanics 44, 441–460.

Calvet, M., Chevrot, S., Souriau, A., Jun. 2006. P-wave propagation in transversely isotropic media: II. Application to inner core anisotropy: Effects of data averaging, parametrization and a priori information. Physics of the Earth and Planetary Interiors 156, 21–40.

Cardin, P., Olson, P., Mar. 1994. Chaotic thermal convection in a rapidly rotating spherical shell: consequences for flow in the outer core. Physics of the Earth and Planetary Interiors 82, 235–259.

804 Côté, A. S., Vočadlo, L., Brodholt, J. P., 2008. Light elements in the core:
805 Effects of impurities on the phase diagram of iron. Geophys. Res. Lett. 35,
806 5306–+.

807 Crank, J., 1984. Free and moving boundary problems. Clarendon Press, Ox-
808 ford UK.

809 Deguen, R., Alboussière, T., Brito, D., 2007. On the presence and structure
810 of a mush at the inner core boundary of the Earth. Phys. Earth Planet.
811 Inter. 274, 1887–1891.

812 Deguen, R., Cardin, P., Jun. 2009. Tectonic history of the Earth's inner core
813 preserved in its seismic structure. Nature Geoscience 2, 419–422.

814 Deguen, R., Cardin, P., 2011. Thermo-chemical convection in the Earth's
815 inner core. Geophysical Journal International, submitted.

816 Deuss, A., Irving, J. C. E., Woodhouse, J. H., May 2010. Regional Variation
817 of Inner Core Anisotropy from Seismic Normal Mode Observations. Science
818 328, 1018–.

819 Dewaele, A., Loubeyre, P., Occelli, F., Mezouar, M., Dorogokupets, P. I.,
820 Torrent, M., 2006. Quasihydrostatic equation of state of iron above 2 mbar.
821 Phys. Rev. Lett. 97, 215504.

822 Dormy, E., Soward, A. M., Jones, C. A., Jault, D., Cardin, P., Feb. 2004.
823 The onset of thermal convection in rotating spherical shells. Journal of
824 Fluid Mechanics 501, 43–70.

825 Dubrovinsky, L., Dubrovinskaia, N., Narygina, O., Kantor, I., Kuznetzov, A.,
826 Prakapenka, V. B., Vitos, L., Johansson, B., Mikhaylushkin, A. S., Simak,
827 S. I., Abrikosov, I. A., 2007. Body-Centered Cubic Iron-Nickel Alloy in
828 Earth's Core. Science 316, 1880–.

829 Dziewonski, A. M., Anderson, D. L., Jun. 1981. Preliminary reference Earth
830 model. Physics of the Earth and Planetary Interiors 25, 297–356.

831 Fearn, D., Loper, D., Roberts, P., 1981. Structure of the Earth's inner core.
832 Nature 292, 232–233.

833 Fearn, D. R., Loper, D. E., Jan. 1981. Compositional convection and strati-
834 fication of earth's core. Nature 289, 393–+.

835 Fiquet, G., Badro, J., Guyot, F., Requardt, H., Krisch, M., 2001. Sound
836 velocities in iron to 100 gigapascals. Science 291, 468–471.

837 Gannarelli, C. M. S., Alfè, D., Gillan, M. J., 2003. The particle-in-cell model
838 for ab initio thermodynamics: implications for the elastic anisotropy of
839 the Earth's inner core. Physics of the Earth and Planetary Interiors 139,
840 243–253.

841 Gannarelli, C. M. S., Alfè, D., Gillan, M. J., Sep. 2005. The axial ratio of
842 hcp iron at the conditions of the Earth's inner core. Physics of the Earth
843 and Planetary Interiors 152, 67–77.

844 Garcia, R., Sep. 2002. Constraints on upper inner-core structure from wave-
845 form inversion of core phases. Geophysical Journal International 150, 651–
846 664.

847 Garcia, R., Souriau, A., Oct. 2000. Inner core anisotropy and heterogeneity
848 level. Geophys. Res. Lett.27, 3121–3124.

849 Ishii, M., Dziewoński, A. M., 2002. The innermost inner core of the earth:
850 Evidence for a change in anisotropic behavior at the radius of about 300
851 km. Proceedings of the National Academy of Science 99, 14026–14030.

852 Jeanloz, R., Wenk, H., Jan. 1988. Convection and anisotropy of the inner
853 core. Geophys. Res. Lett.15, 72–75.

854 Karato, S., Dec. 1993. Inner Core Anisotropy Due to the Magnetic Field-
855 Induced Preferred Orientation of Iron. Science 262, 1708–1711.

856 Karato, S., Dec. 1999. Seismic anisotropy of the Earth's inner core resulting
857 from flow induced by Maxwell stresses. Nature 402, 871–873.

858 Kuwayama, Y., Hirose, K., Sata, N., Ohishi, Y., 2008. Phase relations of iron
859 and iron–nickel alloys up to 300 gpa: Implications for composition and
860 structure of the earth's inner core. Earth and Planetary Science Letters
861 273 (3-4), 379–385.

862 Labrosse, S., Poirier, J.-P., Le Mouël, J.-L., 2001. The age of the inner core.
863 Earth planet. Sci. Lett. 190, 111–123.

864 Laio, A., Bernard, S., Chiarotti, G. L., Scandolo, S., Tosatti, E., Feb. 2000.
865 Physics of Iron at Earth's Core Conditions. Science 287, 1027–1030.

866 Lebensohn, R. A., Tome, C. N., 1993. Self-consistent anisotropic approach
867 for the simulation of plastic deformation and texture development of poly-

crystals: application to zirconium alloys. Acta Metallurgica et Materiala 41, 2611–2624.

Liermann, H.-P., Merkel, S., Miyagi, L., Wenk, H.-R., Shen, G., Cynn, H., Evans, W. J., 2009. New experimental method for in situ determination of material textures at simultaneous high-pressure and ?temperature by means of radial diffraction in the diamond anvil cell. Rev. Sci. Instrum. 80, 104501.

Loper, D. E., 1983. Structure of the inner core boundary. Geophys. and Astrophys. Fluid Dyn. 25, 139–155.

Ma, Y., Somayazulu, M., Shen, G., Mao, H., Shu, J., Hemley, R., 2004. In situ X-ray diffraction studies of iron to Earth-core conditions. Phys. Earth Planet. Inter. 143-144, 455–467.

Mao, H.-K., Shu, J., Shen, G., Hemley, R. J., Li, B., Singh, A. K., Dec. 1998. Elasticity and rheology of iron above 220GPa and the nature of the Earth's inner core. Nature 396, 741–743.

Mao, H. K., Wu, Y., Chen, L. C., Shu, J. F., Jephcoat, A. P., 1990. Static compression of iron to 300 GPa and $Fe_{0.8}Ni_{0.2}$ alloy to 260 GPa: Implications for composition of the core. J. Geophys. Res. 95 (B13), 21737–21742.

Mao, W. L., Struzhkin, V. V., Baron, A. Q. R., Tsutsui, S., Tommaseo, C. E., Wenk, H.-R., Hu, M. Y., Chow, P., Sturhahn, W., Shu, J., Hemley, R. J., Heinz, D. L., Mao, H.-K., 2008. Experimental determination of the elasticity of iron at high pressure. J. Geophys. Res. 113, B09213.

Masters, G., Gubbins, D., Nov. 2003. On the resolution of density within the Earth. Physics of the Earth and Planetary Interiors 140, 159–167.

Merkel, S., Shu, J., Gillet, P., Mao, H.-K., Hemley, R. J., May 2005. X-ray diffraction study of the single-crystal elastic moduli of ϵ-Fe up to 30 GPa. Journal of Geophysical Research (Solid Earth) 110 (9), 5201–+.

Merkel, S., Tomé, C., Wenk, H.-R., 2009. A modeling analysis of the influence of plasticity on high pressure deformation of hcp-co. Phys. Rev. B 79, 064110.

Merkel, S., Wenk, H., Gillet, P., Mao, H., Hemley, R. J., Jul. 2004. Deformation of polycrystalline iron up to 30GPa and 1000K. Physics of the Earth and Planetary Interiors 145, 239–251.

Miyagi, L., Kunz, M., Knight, J., Nasiatka, J., Voltolini, M., Wenk, H., Nov. 2008. In situ phase transformation and deformation of iron at high pressure and temperature. Journal of Applied Physics 104 (10), 103510–+.

Monnereau, M., Calvet, M., Margerin, L., Souriau, A., 2010. Lopsided growth of earth's inner core. Science 328, 1014–1017.

Morelli, A., Dziewonski, A. M., Woodhouse, J. H., 1986. Anisotropy of the inner core inferred from PKIKP travel times. Geophys. Res. Lett. 13, 1545–1548.

Nimmo, F., 2007. Treatise on Geophysics. Vol. 8. Elsevier, Ch. Energetics of the Core, pp. 33–65.

Niu, F., Chen, Q., Oct. 2008. Seismic evidence for distinct anisotropy in the innermost inner core. Nature Geoscience 1, 692–696.

Niu, F., Wen, L., Apr. 2001. Hemispherical variations in seismic velocity at the top of the Earth's inner core. Nature 410, 1081–1084.

Poirier, J. P., Price, G. D., 1999. Primary slip system of ϵ-iron and anisotropy of the Earth's inner core. Phys. Earth Planet. Inter. 110, 147–156.

Poupinet, G., Pillet, R., Souriau, A., 1983. possible heteregeneity of the earth's core deduced from PKIKP travel-times. Nature 305 (5931), 204–206.

Sha, X., Cohen, R. E., 2010. Elastic isotropy of ϵ-fe under earth's core conditions. Geophys. Res. Lett. 37, L10302.

Shimizu, H., Poirier, J.-P., Le Mouël, J.-L., 2005. On crystallization at the inner core boundary. Phys. Earth Planet. Inter. 151, 37–51.

Song, X., Helmberger, D. V., Jun. 1995. Depth dependence of anisotropy of Earth's inner core. J. Geophys. Res.100, 9805–9816.

Souriau, A., Jan. 2003. The seismological picture of the inner core: structure and rotation. Comptes Rendus Geoscience 335, 51–63.

Souriau, A., 2007. Treatise on Geophysics. Vol. 1. Elsevier, Ch. The Earth's Core, pp. 655–693.

Souriau, A., Poupinet, G., Nov. 1991. The velocity profile at the base of the liquid core from PKP(BC+Cdiff) data: An argument in favor of radial inhomogeneity. Geophys. Res. Lett.18, 2023–2026.

933 Souriau, A., Romanowicz, B., 1996. Anisotropy in inner core attenuation: a
934 new type of data to constrain the nature of the solid core. Geophys. Res.
935 Lett. 23, 1–4.

936 Souriau, A., Romanowicz, B., Apr. 1997. Anisotropy in the inner core: rela-
937 tion between P-velocity and attenuation. Physics of the Earth and Plane-
938 tary Interiors 101, 33–47.

939 Stacey, F., Davis, P., 2008. Physics of the Earth. Cambridge University Press,
940 Cambridge UK.

941 Stacey, F., Loper, D., 2007. A revised estimate of the conductivity of iron
942 alloy at high pressure and implications for the core energy balance. Phys.
943 Earth Planet. Inter. 161, 13–18.

944 Stacey, F. D., Anderson, O. L., 2001. Electrical and thermal conductivities
945 of Fe-Ni-Si alloy under core conditions. Phys. Earth Planet. Inter. 124,
946 153–162.

947 Steinle-Neumann, G., Stixrude, L., Cohen, R. E., Gülseren, O., Sep. 2001.
948 Elasticity of iron at the temperature of the Earth's inner core. Nature 413,
949 57–60.

950 Stixrude, L., Cohen, R. E., Mar. 1995. High-Pressure Elasticity of Iron and
951 Anisotropy of Earth's Inner Core. Science 267, 1972–1975.

952 Su, W., Dziewonski, A. M., Jeanloz, R., Dec. 1996. Planet Within a Planet:
953 Rotation of the Inner Core of Earth. Science 274, 1883–1887.

954 Sumita, I., Olson, P., 1999. A Laboratory Model for Convection in Earth's
955 Core Driven by a Thermally Heterogeneous Mantle. Science 286, 1547–
956 1549.

957 Sumita, I., Olson, P., Aug. 2002. Rotating thermal convection experiments in
958 a hemispherical shell with heterogeneous boundary heat flux: Implications
959 for the Earth's core. Journal of Geophysical Research (Solid Earth) 107,
960 2169–+.

961 Sumita, I., Yoshida, S., Kumazawa, M., Hamano, Y., 1996. A model for
962 sedimentary compaction of a viscous media and its application to inner-
963 core growth. Geophys. J. Int. 124, 302–324.

964 Tanaka, S., Hamaguchi, H., Feb. 1997. Degree one heterogeneity and
965 hemispherical variation of anisotropy in the inner core from PKP(BC)-
966 PKP(DF) times. J. Geophys. Res.102, 2925–2938.

967 Tome, C., Canova, G., Kocks, U., Christodoulou, N., Jonas, J., 1984. The
968 relation between macroscopic and microscopic strain hardening in f.c.c.
969 polycrystals. Acta Metallurgica 32 (10), 1637 – 1653.

970 Turcotte, D. L., Schubert, G., 2002. Geodynamics. pp. 472. ISBN
971 0521661862. Cambridge, UK: Cambridge University Press.

972 Van Orman, J. A., 2004. On the viscosity and creep mechanism of Earth's
973 inner core. Geophysical Research Letters 31, 20606–+.

974 Vočadlo, L., 2007. Treatise on Geophysics. Vol. 2. Elsevier, Ch. The Earth's
975 Core: Iron and Iron Alloys, pp. 91–120.

976 Vočadlo, L., Alfè, D., Gillan, M. J., Wood, I., Brodholt, J., Price, G. D.,
977 2003. Possible thermal and chemical stabilization of body-centred-cubic
978 iron in the Earth's core. Nature 424, 536–539.

979 Vočadlo, L., Dobson, D. P., Wood, I. G., Nov. 2009. Ab initio calculations of
980 the elasticity of hcp-Fe as a function of temperature at inner-core pressure.
981 Earth and Planetary Science Letters 288, 534–538.

982 Weber, P., Machetel, P., Nov. 1992. Convection within the inner-core and
983 thermal implications. Geophys. Res. Lett.19, 2107–2110.

984 Wenk, H., Baumgardner, J. R., Lebensohn, R. A., Tomé, C. N., Mar.
985 2000. A convection model to explain anisotropy of the inner core. J. Geo-
986 phys. Res.105, 5663–5678.

987 Wenk, H. R., 1999. A voyage through the deformed earth with the self-
988 consistent model. Model. Simul. Mater. Sci. Engin. 7, 699–722.

989 Wenk, H. R., Matthies, S., Hemley, R. J., Mao, H. K., Shu, J., 2000. The
990 plastic deformation of iron at pressures of the Earth's inner core. Nature
991 405, 1044–1047.

992 Wenk, H. R., Takeshita, T., Jeanloz, R., Johnson, G. C., Jan. 1988. Develop-
993 ment of texture and elastic anisotropy during deformation of hcp metals.
994 Geophys. Res. Lett.15, 76–79.

995 Woodhouse, J. H., Giardini, D., Li, X.-D., 1986. Evidence for inner core
996 anisotropy from free oscillations. Geophys. Res. Lett. 13, 1549–1552.

997 Worster, M. G., 1997. Convection in Mushy Layers. Annual Review of Fluid
998 Mechanics 29, 91–122.

999 Yoshida, S., Sumita, I., Kumazawa, M., Dec. 1996. Growth model of the
1000 inner core coupled with the outer core dynamics and the resulting elastic
1001 anisotropy. J. Geophys. Res.101, 28085–28104.

1002 Yu, W., Wen, L., May 2006a. Inner core attenuation anisotropy. Earth and
1003 Planetary Science Letters 245, 581–594.

1004 Yu, W., Wen, L., Jul. 2006b. Seismic velocity and attenuation structures in
1005 the top 400 km of the Earth's inner core along equatorial paths. Journal
1006 of Geophysical Research (Solid Earth) 111, 7308–+.

1007 Zhang, K., Mar. 1992. Spiralling columnar convection in rapidly rotating
1008 spherical fluid shells. Journal of Fluid Mechanics 236, 535–556.